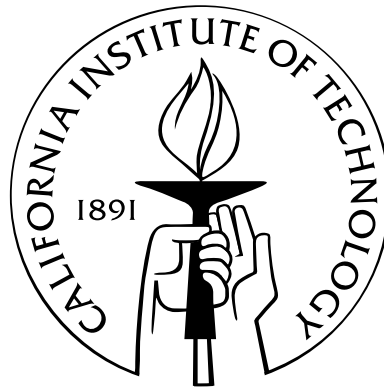


A Constitutive Relation for Shape-Memory Alloys

Thesis by

Alex Kelly

In Partial Fulfillment of the Requirements
for the Degree of
Doctor of Philosophy



California Institute of Technology
Pasadena, California

2009

(Defended September 4, 2008)

© 2009

Alex Kelly

All Rights Reserved

Acknowledgements

It would cheapen the pure sentiment of gratitude that I wish to express in this section to fill it with cringe-inducing metaphors about birds flying for the first time or pithy quotes from philosophers of bygone centuries. Instead, I would like to thank those people who have lent to me the best of themselves in spite of the fact that I did not deserve it.

Michael Kelly

Sheila Kelly

Evan Kelly

Jared Kelly

Kaushik Bhattacharya

Richard Murray

Jenni Buckley

Alexis Cox

Meher Kiran Prakash Ayalasomayaajula

Patrick Dondl

Kaushik Dayal

Samantha Daly

Amir Sadjadpour

Lixiu Tian

Vikram Gavini

Phanish Suryanarayana

Isaac Chenchiah

Mathias Jungen

Sefi Givli

Christian Lexcellent

Guruswami Ravichandran

Sylvie Gertmenian

Abstract

The novel nonlinear thermoelastic behavior of shape-memory alloys (SMAs) makes them increasingly desirable as components in many advanced technological applications. In order to incorporate these materials into engineering designs, it is important to develop an understanding of their constitutive response. The purpose of this thesis is to develop a constitutive model of shape-memory polycrystals that is faithful to the underlying micromechanics while remaining simple enough for utility in engineering analysis and design.

We present a model in which the material microstructure is represented macroscopically as a recoverable transformation strain that is constrained by the texture of the polycrystal. The point of departure in this model is the recognition that the mechanics of the onset of martensitic transformation are fundamentally different from those of its saturation. Consequently, the constraint on the set of recoverable strains varies throughout the transformation process. The effects of constraint geometry on the constitutive response of SMAs are studied. Several well known properties of SMAs are demonstrated. Finally the model is simply implemented in a commercial finite-element package as a proof of the concept.

Contents

Acknowledgements	iii
Abstract	iv
Contents	v
List of Figures	vii
1 Introduction	1
2 Background	7
2.1 Review	7
2.1.1 Crystallography	7
2.1.2 Mathematical Background	9
2.1.3 Experiments	12
2.1.4 Homogenization Literature	13
2.1.5 Kinetics	16
2.1.6 Constitutive Modelling	16
2.2 Motivation	19
3 Continuum Model	22

3.1	Kinematics	22
3.2	Balance Laws	24
3.3	Energy	27
3.4	Initiation and Saturation	29
3.5	Driving Forces and Kinetics	35
4	Some Features of the Model	41
4.1	One Dimension	41
4.1.1	Stress-Induced Martensite	41
4.1.2	Shape-Memory Effect	46
4.2	Martensite Reorientation	49
5	Demonstration and Parameter Study	51
5.1	Uniaxial Tension and Compression	52
5.2	Simple Shear	56
5.3	Combined Uniaxial Extension and Shear	58
5.4	Anisotropic Materials	61
5.5	Proportional Loading in Different Directions	63
5.6	Nonproportional Loading	68
6	Numerical Implementation and Example	73
7	Conclusions and Future Directions	80
	Bibliography	83

List of Figures

1.1	A schematic representation of superelasticity in a specimen above A_f	2
1.2	A schematic representation of the shape-memory effect	4
1.3	A picture showing a) coronary stent (Nitinol Devices and Components Inc.), b) schematic of a compressed stent inserted into a hollow structure and expanded. (from http://openlearn.open.ac.uk).	5
2.1	Austenite and variants of the low symmetry martensite in the continuum	9
2.2	Polycrystalline specimens have the added wrinkle of intergrain compatibility	11
2.3	Polarized Light Micrographs by Brinson et al. [19] at a) onset of transformation and b) saturation	14
3.1	The volume fraction and the nominal effective strain are constrained to lie in the identified set.	25
3.2	A schematic representation of sets $\mathcal{G}_{i,s}$	26
3.3	A schematic representation of the first two terms of W	28
3.4	The degree of tension-compression asymmetry of the initiation and saturation surfaces is adjusted through the parameter b	30

3.5	The degree of eccentricity of the initiation and saturation surfaces is varied through the parameter c . The effects of variation of this parameter are seen on a) a symmetric set, and b) a set with a high degree of asymmetry.	31
3.6	The direction of eccentricity is controlled through variation of the vector \hat{e} . The effects of variation of this parameter are seen on a) a symmetric set, and b) a set with a high degree of asymmetry.	32
3.7	A suitable choice of parameters for the set of admissible transformation strains (a) allows for recovery of the tension-compression asymmetry in the biaxial experiments in the dual stress space (b). A more precise fit to the experimental data was proposed by Lexcellent in d) and its strain-space dual in c).	34
3.8	The kinetic relation governing the phase transition in the stick-slip case.	39
4.1	Stress-induced martensite in one dimension shown in the volume fraction-strain plane on the left and the stress-strain plane on the right. The constraints on the volume fraction and nominal transformation strain are indicated on the shaded set.	42
4.2	Shape-memory effect in one dimension shown in the the volume fraction-strain plane on the left and the stress-strain-temperature space on the right. The constraints on the volume fraction and nominal transformation strain are indicated on the shaded set.	46
4.3	The different eccentricities of the set \mathcal{G}_i and \mathcal{G}_s can lead to a significant reorientation of the martensite. The nominal transformation strain at different extents of transformation is shown.	48

- 5.1 A proportional strain-controlled extension-shear test of an isotropic material. (a) The resulting stress, (b) the resulting transformation strain along with a verification of the numerical method, (c) uniaxial stress vs. uniaxial strain (d) shear stress vs. shear strain and (e) equivalent stress vs. equivalent strain. 60
- 5.2 Anisotropy of the initiation surface. Combined extension and shear of an uniaxial material under strain control for various values of c_i ranging from 0.3-1.5. (a) The effective transformation strain trajectory. The applied strain trajectory is indicated by the dashed line. (b) The stress trajectory, (c) equivalent stress vs. equivalent strain (d) volume fraction vs. equivalent strain. 62
- 5.3 Anisotropy of the saturation surface. Combined extension and shear of an uniaxial material under strain control for various values of c_s ranging from 0.3 to 1.5. (a) The effective transformation strain trajectory. The applied strain trajectory is indicated by the dashed line. (b) The stress trajectory, (c) equivalent stress vs. equivalent strain, (d) volume fraction vs. equivalent strain. 64
- 5.4 Anisotropy of the both surfaces. Combined extension and shear of an uniaxial material under strain control for various values of c_i, c_s ranging from 0.3 to 1.5 (in equal increments). (a) The effective transformation strain trajectory. The applied strain trajectory is indicated by the dashed line. (b) The stress trajectory, (c) equivalent stress vs. equivalent strain, (d) volume fraction vs. equivalent strain. 65

5.5	Variation of direction applied strain. (a) The effective transformation strain trajectory. The applied strain trajectories are indicated by the dashed lines. (b) The stress trajectory, (c) equivalent stress vs. equivalent strain, (d) volume fraction vs. equivalent strain.	66
5.6	Variation of direction applied stress. (a) The effective transformation strain trajectory. (b) The stress trajectory, (c) equivalent stress vs. equivalent strain, (d) volume fraction vs. equivalent strain.	67
5.7	The experimental observations of Jung [36] show the emergence of secondary hysteresis in nonproportional tension-torsion.	68
5.8	Dual plateau in nonproportional loading. (a) The effective transformation strain trajectory. The applied strain trajectories are indicated by the dashed lines. (b) The stress trajectory, (c) equivalent stress vs. equivalent strain, (d) volume fraction vs. equivalent strain.	69
5.9	Circular Loading Path. (a) The effective transformation strain trajectory. The applied strain trajectories are indicated by the dashed lines. (b) The stress trajectory, (c) equivalent stress vs. equivalent strain, (d) volume fraction vs. equivalent strain.	71
5.10	Square Loading Path. (a) The effective transformation strain trajectory. The applied strain trajectories are indicated by the dashed lines. (b) The stress trajectory, (c) equivalent stress vs. equivalent strain, (d) volume fraction vs. equivalent strain.	72
6.1	The Legendre transform of the dissipation potentials are shown in the stick-slip case (black) for $p = 2$ and in the rate-independent case (red).	75

6.2	The effect of the polynomial constraint is seen. The intersection of the 16th degree polynomial shifts the intersection point with the quadratic elastic energy slightly to the right of the hard (dashed) constraint. . . .	76
6.3	The smoothed constraint set is calculated at 10% applied strain. The green dashed constraint is \mathcal{G}_s , the red dashed constraint is the scaled \mathcal{G}_s at $\lambda = \lambda_{sat}$ and the red solid set is the softened polynomial (N = 16) constraint at λ_{sat}	77
6.4	A flowchart of the numerical implementation	78
6.5	An example of the finite-element implementation on a stent element. .	79

Chapter 1

Introduction

Shape-memory alloys (SMAs) exhibit special macroscopic phenomena including superelasticity and the shape-memory effect. In superelasticity, strains on the order of a few percent can be induced by loading and are completely recovered on unloading. In shape-memory, a sample deformed apparently permanently by a few percent strain below a particular critical temperature returns to its original shape upon heating. SMAs have been employed in a large number of engineering applications in fields ranging from medicine to telecommunications. Due to their importance in established and developing engineering fields, a vast literature has risen to study these materials. Volumes by Olson and Owen [45], Otsuka and Wayman [46], and Bhattacharya [12] as well as the review of Saburi and Nenno [52] provide an accessible introduction to the development of experiments and theories used to characterize these important alloys.

The special phenomena arise as a result of the existence of two solid phases in a shape-memory alloy. These phases, rearrangements of the alloy's crystal lattice, are characterized by the lattice symmetry group. The high symmetry phase, austenite, is generally stable at high temperatures; with the lower symmetry phase, martensite, stable at lower temperatures. As an example in NiTiNOL, the most celebrated of

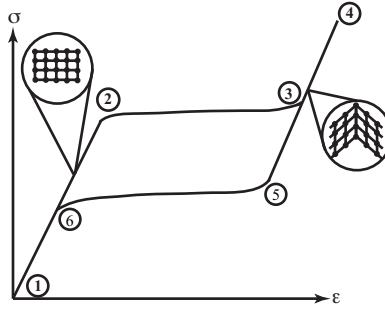


Figure 1.1: A schematic representation of superelasticity in a specimen above A_f .

the SMAs, the austenite is cubic with monoclinic martensite. The change between the two phases is a first-order diffusionless transformation that can be activated by changes in either temperature or stress. At zero stress, the phase transition is characterized by four temperature points: the Martensite start (M_s) at which a sample that is completely austenite begins forming martensite, Martensite finish (M_f) is the temperature at which the austenite-martensite transformation saturates, the Austenite start (A_s) at which a completely martensitic sample begins forming austenite, and the Austenite finish (A_f) is the temperature at which the martensite-austenite transformation reaches completion. The possibility of large atomic scale displacement in the sample contributes to highly nonlinear thermoelastic behavior on the macro scale.

Superelasticity is the ability of the sample to recover large strains elastically. The magnitude of elastic strains recovered in superelastic SMAs is quite impressive. Whereas a typical metal recovers strains on the order of 0.2 %, a sample of NiTiNOL demonstrates recovery of somewhere between 6% and 8%. For a constant temperature above the austenite finish (A_f) the stress-strain behavior of a superelastic material is shown schematically in figure 1.1.

The initial branch of the hysteresis loop (between points 1 and 2) is the elastic

response of the austenite. When a threshold stress is reached (point 2) the formation of martensite is induced. The atomic displacement that accompanies the change in phase allows for large strains to accumulate as the austenite-martensite transformation continues. At point 3 the martensitic transformation has saturated and the martensite responds elastically to the extent that it can before failure (point 4). Unloading sees the formation of the lower branch of the hysteresis loop. The martensite unloads elastically until point 5. At this point, the free energy is low enough that the transformation back to the stable austenite begins. When the transformation back to austenite finishes (point 6), unloading finishes elastically (back to point 1). It is worth noting that the entire amount of strain is recovered during the loading-unloading cycle because the phase transformation is an reversible distortion of the crystal lattice, and no breaking of bonds has occurred (in a lattice free of defects).

The second characteristic phenomenon resulting from the martensitic phase transformation is the shape-memory effect. In order for the crystal to remain intact after it has undergone a phase transformation, recall that it must satisfy the Hadamard-Legendre conditions at each interface between martensite variants with each other or with the austenite. These jump conditions lead to the formation of self-accommodating (no change in volume) microstructure in the SMA crystal as different variants of martensite must mix coherently in order to preserve the integrity of the crystal. It is this formation of microstructure that is responsible for the shape-memory effect.

As can be seen in figure 1.2, the considered transformation begins with a completely austenite reference configuration in the high temperature regime. As the specimen cools and martensitic variants become more energetically favorable a self-accommodating microstructure forms. As the cooled specimen is deformed, the phase fraction of martensitic variants is changed via stress-induced transformation and the resulting microstructure is different in the deformed configuration. Upon heating of

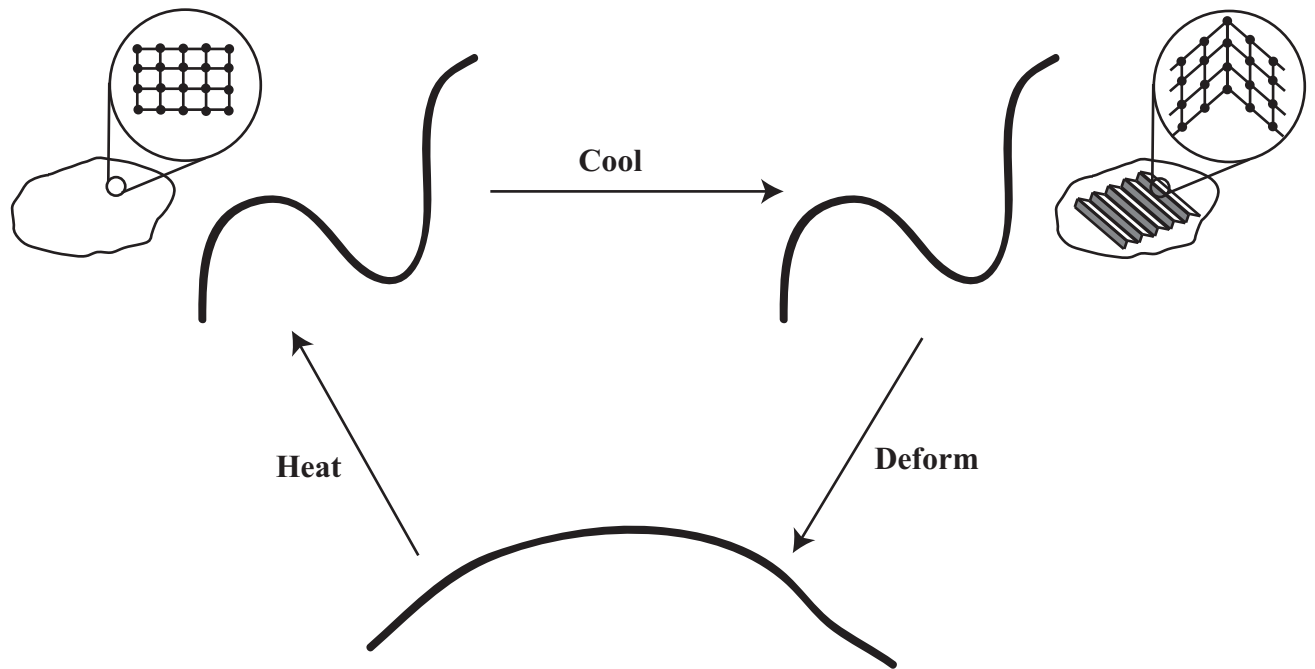


Figure 1.2: A schematic representation of the shape-memory effect

the sample, austenite once again becomes the energetically favorable phase, and as a result the reference configuration is restored as the crystal returns to the austenite lattice. The sample has recovered its reference configuration through the change in phase, hence shape "memory".

Shape-memory alloys are used in many devices. Biomedical devices such as stents and braided catheters take advantage of the superelasticity of SMAs. The ability of the alloy to recover large strains elastically allows for expandable structures to be compressed down to very small sizes and delivered into an obstructed passage. allows for the obstructions to be circumvented without recourse to invasive surgeries. The stent, shown in figure 1.3, is a cylindrical wire mesh structure that is compressed to fit around an insertion tube or catheter. The compressed stent is inserted on the catheter into an obstructed (by arterial plaque) blood vessel and expanded via

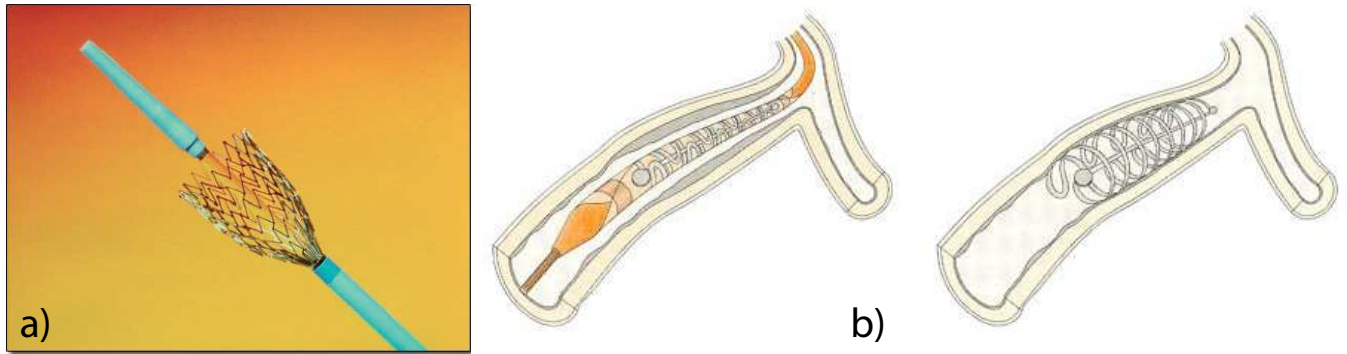


Figure 1.3: A picture showing a) coronary stent (Nitinol Devices and Components Inc.), b) schematic of a compressed stent inserted into a hollow structure and expanded. (from <http://openlearn.open.ac.uk>).

balloon. Because the stent is able to recover the large strain required for insertion, it is able to hold the blocked vessel open.

Shape-memory is applied in the aerospace field, particularly in deep-space actuators such as latches where traditional moving parts would be a riskier method of achieving the desired actuation than the thermomechanical capability of the SMA ([42], for example, shows one such example in the case of unfolding solar panels on the Hubble Space Telescope). For further information on a wide variety of applications, the reader is referred to [34] and the references within.

As the applications of SMAs grow more sophisticated, there is a real need to develop a faithful yet easy-to-use constitutive model that can be used as a design tool. This is the motivation for this thesis. The plan for the thesis is as follows:

In chapter 2, the existing literature in both mathematical theory and experiments is examined. This literature review is undertaken with the purpose of underscoring some of the important open issues in the understanding of shape-memory alloys. The examination of these open issues results in the proposal of a heuristic that defines the mechanics of onset and saturation of martensitic transformation in shape-memory

polycrystals as distinctly different processes.

Chapter 3 contains the incorporation of this heuristic into a continuum model. The onset and saturation heuristics are manifest in this model as a pair of constraints on the set of admissible transformation strains resulting from the formation of microstructure in the polycrystal. These constraints are vital to the formulation of a polycrystalline Helmholtz free energy that, along with an appropriate dissipation potential, yields the proposed continuum model with few internal variables.

The ability of the proposed continuum model to duplicate the well-known characteristics of SMAs is evaluated in chapter 4. The continuum model in the third chapter is shown to reproduce superelasticity and the shape-memory effect. Experimental observation of martensitic reorientation and retention of austenite are accounted for as well.

The constraints that form the backbone of the proposed model undergo parameter studies in numerical simulations in chapter 5. When the shape of the constraint surfaces is varied parametrically, a large variability in the resultant constitutive response demonstrates the potential of the model to be fit to a large number of important experiments. An explanation is offered for the curious observations of Jung [36] in non proportional tension-torsion experiments on Nitinol tubes.

Finally, in chapter 6 the model is incorporated into a commercial finite element package as an ABAQUS UMAT. This is done in order to demonstrate the relative ease of implementation of this model as a feasible design tool for engineering applications.

Chapter 7 summarizes this thesis and provides a discussion of open issues and future research.

Chapter 2

Background

2.1 Review

2.1.1 Crystallography

The crystal lattice of a shape-memory alloy is assumed to undergo transformation from a high symmetry austenite phase (stable at higher temperatures) to a lower symmetry martensite (stable at lower temperatures). Mathematically the crystal is described as a Bravais lattice with basis vectors $\{e_1, e_2, e_3\}$. For simplicity's sake, it is assumed that these basis vectors coincide with the high symmetry austenite phase. Assume that the martensite (low symmetry) phase is described by a different set of basis vectors $\{f_1, f_2, f_3\}$. The two bases are related by a matrix transformation \mathbf{A} :

$$[f_1, f_2, f_3] = \mathbf{A} [e_1, e_2, e_3]. \quad (2.1)$$

Recalling that the matrix \mathbf{A} can be decomposed by the Polar Decomposition Theorem into a rotation \mathbf{Q} and a symmetric positive definite matrix \mathbf{U} such that $\mathbf{A} = \mathbf{Q}\mathbf{U}$. The rotation is irrelevant to the energy landscape of the lattice due to the require-

ment that it be materially frame indifferent. This being the case, the martensite is characterized by the Bain or transformation matrix \mathbf{U} . The variants of martensite are then easily found by symmetry through application of point group of the austenite phase (for example the cubic point group in nickel-titanium). For each rotation \mathbf{R}_i in the point group of the austenite, the transformation matrix for the martensitic variant \mathbf{U}_i is found by:

$$\mathbf{U}_i = \mathbf{R}_i^T \mathbf{U} \mathbf{R}_i. \quad (2.2)$$

It is worth noting that application of rotations \mathbf{R}_i that are also in the point group of the martensite (monoclinic in the case of NiTi) do not produce a new variant. The number of unique variants then can be shown to be $\frac{P_a}{P_m}$ where P_a is the cardinality of the point group of the austenite, and P_m that of the martensite.

The Helmholtz free energy for the crystal takes the form of a multiwell energy with wells at the unique austenite (\mathbf{I}) as well as each of the martensite \mathbf{U}_i lattice deformations. This multiwell structure goes back to Ericksen [29]. The relative heights of the austenite and martensite wells change generally with temperature to reflect the stability of each phase with respect to some critical temperature. The transition is usually of first order in the language of Landau free energies.

The connection between the lattice picture and the continuum is made through the Cauchy-Born hypothesis [9]. Matrix deformations of the bravais lattice basis vectors are assumed to be written in the continuum as deformation gradients. The austenite phase is represented as the deformation gradient \mathbf{I} . The martensites are represented by the corresponding deformation gradients \mathbf{U}_i . The multiwell Helmholtz free energy for the single crystal in the continuum can be represented schematically as $W_{sc}(\mathbf{F})$ in figure 2.1. In the small strain approximation, the austenite is at zero strain ($\varepsilon = 0$), and the wells associated with each variant are $\varepsilon_i = U_i - I$.

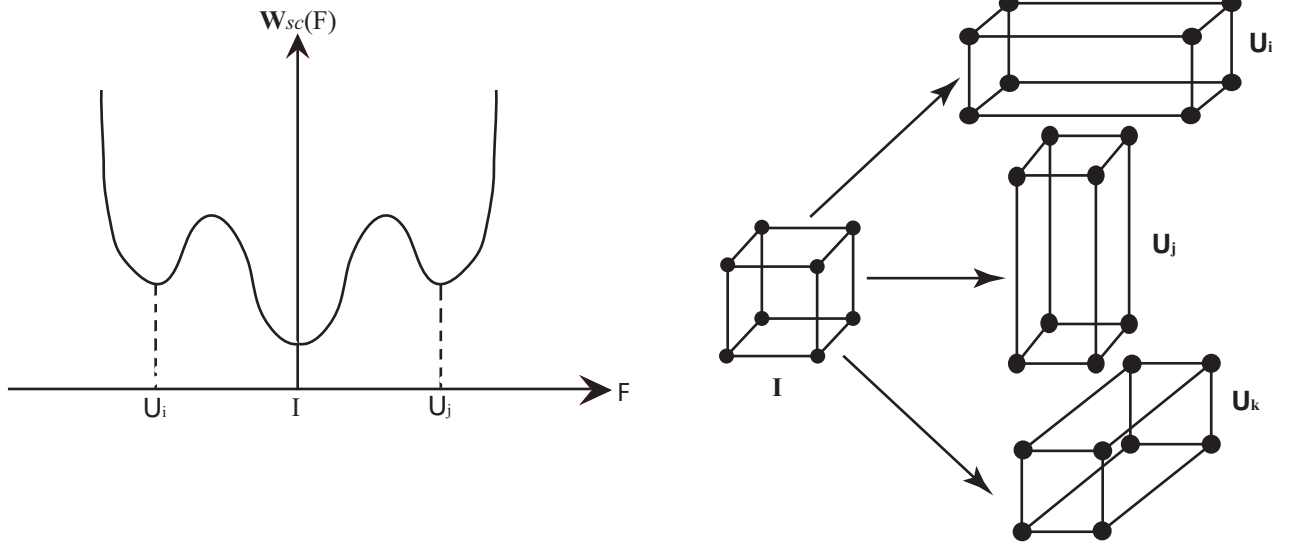


Figure 2.1: Austenite and variants of the low symmetry martensite in the continuum

2.1.2 Mathematical Background

The most striking feature of the multiwell Helmholtz Free Energy described above is its nonconvexity. The nonconvexity of the energy introduces complications in understanding of the material's macroscopic response. Ball and James [8] recognized that microstructures form in these multiwell materials as a consequence of their nonconvex energies. This was independently concluded by Chipot and Kinderlehrer [24]. These microstructures, essentially mixtures of the low energy phases arranged in such a way as to reduce the energy penalties associated with kinematic incompatibility, lead to overall "relaxed" energies that are lower than the multiwell ones. However, precise characterizations of these relaxed energies is a difficult analytical problem.

The proper analytical setting for the relaxation of energies is weak lower semi-continuity. It has been known for some time [44] that a necessary and sufficient condition for weak lower semi-continuity is quasiconvexity. Quasiconvexity is a non-

local property. Consequently, it is in general difficult to calculate the quasiconvex hulls of these multiwell free energies. It is possible to more easily bound the quasiconvex hulls from above and below. Ball [6] developed the notion of polyconvexity, and the polyconvex hull is an upper bound to the quasiconvex hull. From below, the quasiconvex hull is bounded by the rank-one convex hull. The relation between rank-one convexity and quasiconvexity is not completely understood. For functions in space dimensions greater than two Sverak [63] has constructed a rank-one convex function that is not quasiconvex. The problem of whether such a function exists in the plane is still open.

It is worth mentioning that some special cases of quasiconvex hulls have been found. The two-well problem has been fairly thoroughly examined. Ball and James ([9]) found the zero energy set of two nonlinear, compatible wells. Kohn addressed the case of two linear wells [37] of equal modulus, as did Pipkin [49]. Chenchiah [23] extended these results to the case of two linear wells of possibly unequal moduli. Bhattacharya [10] found the hull of multiple, pairwise compatible, linear wells of equal modulus. Govindjee et al. [33] estimated a lower bound in the case of many wells by constructing a pairwise quasiconvex hull.

More difficulty arises in the case of the martensitic polycrystal. One has to account for the relaxation of the multiwell energy within each of the grains as well as intergrain compatibility problems that arise from the orientations of the different grains. The work of Bruno et al.[21] focuses on the effects of this intergranular interaction. By treating each grain as an isolated circular inclusion transforming in an elastic medium, the elastic field of each transforming grain is found using Eshelby [30] solutions. These solutions are easily superposed. The elastic response of the "polycrystal" is examined by finite dimensional minimization of the energy of each grain. A similar line of inquiry that attempts to incorporate more of the grain

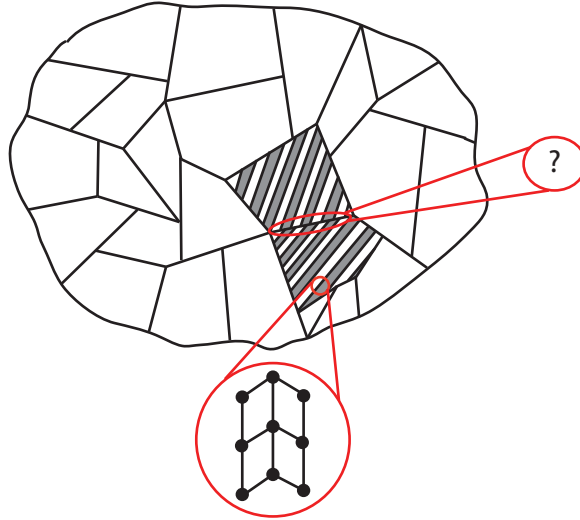


Figure 2.2: Polycrystalline specimens have the added wrinkle of intergrain compatibility

geometry was conducted by Patoor and co-workers [47]. The grains in this model are no longer treated as isolated from each other in their analysis. The analysis is still conducted by using Eshelby inclusions. The elastic energy contributed by the transforming inclusions is found by superposition. The result of these calculations is a quadratic transformation energy that is easily incorporated into an FEM model. These Eshelby-type calculations, though attractive for their relative computational simplicity, serve only as a starting point for polycrystalline analysis. They generally skirt the complex issues of microstructural formation and granular interactions.

2.1.3 Experiments

The mathematical analysis of microstructures in shape-memory polycrystals is maturing quickly. It remains, however, largely incapable of a precise characterization of their macroscopic response in general. A parallel pursuit has been to attempt to characterize the mechanisms of shape-memory and superelasticity experimentally. A fairly thorough review of the historical development of this experimental literature in single crystals is in the book of Otsuka and Wayman [46]. This thesis is more interested in the recent systematic experimental examination of these phenomena in polycrystals. Experimentally it has been known for some time that the texture of a polycrystal drastically effects its elastic response. This was demonstrated in 1990 [31] in the case of rolled sheets of nickel-titanium in uniaxial tension tests. The results of Daly et al. [26] reinforce this strong textural dependence in thin sheets of NiTiNOL. The failure of the resolved shear stress criterion for polycrystals, observed in their experiments, indicates that the mechanics of onset of transformation in polycrystals is highly sensitive to load orientation with respect to the sample texture.

A systematic examination of the response of shape-memory polycrystals in multiple loading modes is required to completely explain the effect of texture. LExcellent et al. [41, 39] conducted a detailed investigation of the onset of transformation in Nickel-Titanium, Cu-Zn-Al, Cu-Al-Ni and Cu-Al-Be alloys in biaxial proportional loading. These investigations allowed for the formulation of yield surface for transformation in the stress space. Sittner's experiments [59] in 1995 similarly illuminated the anisotropy of onset mechanics in combined loading. The experiments of Shaw and Kyriakides [56] among others ([32],[26]) indicate that the onset of transformation is a local mechanism. The observed domains of martensite in thin sheets and thin-walled tubes tend to nucleate in bands that widen and propagate throughout

the sample until transformation saturates.

The experimental examination of the onset of transformation is interesting. An understanding of the saturation of transformation is required to complete the story. The experimental observations of Jung et al. ([36, 43]) on mixed-mode loading of NiTiNOL tubes reveal that there are interesting mechanics still to be resolved after the onset of transformation. The observation of secondary hysteresis loops in tension after saturation of the transformation in tension indicated that the saturation process was also anisotropic. In addition, the saturation does not proceed until the sample is completely martensitic (unlike in the single crystal case); loading in torsion was able to increase the total amount in martensite in the sample after the transformation was saturated in tension.

The in situ microscopy experiments by Brinson et al. ([19, 55]) on polycrystalline Nickel-Titanium lend some insight into the mechanics of phase transitions from onset all the way to saturations. These experiments confirm the local nature of the initiation of transformation. Islands of martensite are seen nucleating in isolated grains in the elastic austenite. The saturation of the transformation is arrested with large interlocking "fingers" of martensite oriented in the same direction. At saturation these experiments clearly demonstrate that the intergranular constraints arrest the transformation process before completion. The saturation occurs at martensitic phase fractions between 60% and 70 % in these tests.

2.1.4 Homogenization Literature

The important class of "yield surface" constitutive models were introduced purely phenomenologically. An important question to ask when considering their connection to underlying micromechanics is whether they can be reconciled with existing

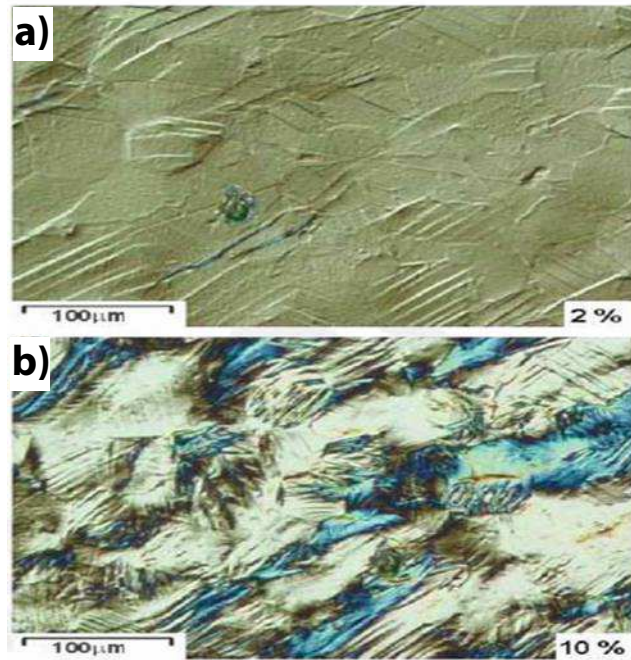


Figure 2.3: Polarized Light Micrographs by Brinson et al. [19] at a) onset of transformation and b) saturation

ideas in the mathematical literature, and whether these ideas can be used to improve the models. The total recoverable strain of a polycrystal is something that has been examined in some detail in the homogenization literature. The work of Kohn and Bhattacharya [13] attempted to determine the the total recoverable strain of polycrystals with certain microstructures and textures. They demonstrate that the Taylor (or constant strain) bound is usually a good approximation of the total recoverable strain. This work was a novel use of the Taylor bound that has its origin in the crystal plasticity literature (for example Kohn and Little [38] and the references therein). Bhattacharya and Shu [58] expanded on the framework set out by Kohn and Bhattacharya, examining the effect of polycrystalline texture, in the case of compatible and incompatible martensitic variants, on shape-memory in multiaxial loading cases. The importance of the Taylor and constant stress (Sachs) bound on the response of polycrystal has led Schlömerkemper [54] and Schlömerkemper and Bhattacharya [15] to characterize them in various cases. Among the interesting revelations of these works was the striking difference in the shape of the Taylor and Sachs bounds for a given microstructure in many cases.

An alternative to placing bounds on the total recoverable strain of the polycrystal by determination of the Taylor set was proposed by Smyshlyaev and Willis [60]. The formulation of a Hashin-Shtrikman variational principle is presented in terms of grain statistics (particularly the two-point statistics of the polycrystal). An upper bound of the total recoverable strain can be derived from the Hashin-Shtrikman variational principle in the case of the statistically uniform polycrystal.

2.1.5 Kinetics

The experimental observations of Shaw and Kyriakides [56] and Brinson et al. [19] indicate that the martensitic transformation is a process that begins locally and advances through the propagation of one or many phase boundaries. In order to close a constitutive model in the sense of [3], a kinetic law(s) for the volume fraction of martensite (or each variant of martensite) is required. In an attempt to understand how such kinetic laws might be derived, the study of the advancement of phase boundary in continua has been a subject of keen interest. The propagation of phase boundaries is thought to be due to a combination of metastability and pinning ([2, 11, 14]). The effect of pinning was investigated in some detail by Dondl ([28]) who found a universal power law between phase boundary speed and driving traction. Dayal and Bhattacharya [27] had some success in numerically deriving a stick-slip kinetics in a double well material through the use of peridynamics.

2.1.6 Constitutive Modelling

In order to incorporate these experimental observations into the design process, it is necessary to derive constitutive model for their material response. Several attempts have been made historically to incorporate the key mechanisms of shape-memory into a constitutive framework. Abeyaratne and Knowles [4] developed a generic thermo-mechanical model for a phase-transforming solid. This model featured a Helmholtz free energy dependent on the martensitic phase fraction, a nucleation condition for martensitic growth, and a kinetic law for the transformation process in one dimension. More continuum models followed in this general mold. Sun and Hwang [61] developed a micromechanics inspired free energy to reproduce the superelasticity and shape-memory effect under uniaxial loading. Boyd and Lagoudas [17] developed a

Helmholtz free energy and dissipation potential for isotropic shape-memory alloys. A final significant uniaxial, micromechanical model worthy of examination is that of Huang and Brinson [35]. This uniaxial model in three dimensions considers the formation of self-accommodating groups of martensite variants as a mode of energy minimization. Tracking the formation of these energy-minimizing groups, the model is able to accurately capture the uniaxial response of single crystals in uniaxial loading. Brinson et al. [20] also developed a three-dimensional constitutive model based on the notion of microplanes.

An alternative approach in the three-dimensional case was introduced by Auricchio and Taylor [5]. The model, incorporating an idea from the plasticity literature, uses a "yield surface" in the space of stress for the onset of phase transformation. The yield surface is determined by fitting several uniaxial experiments in different directions. As such it is not derived from a coherent micromechanics. However, it has been quite successful in simplifying the computational implementation of SMA response in commercial finite-element packages [1]. LExcellent and his collaborators ([39, 41]) developed a micro-macro constitutive model in this vein. Their numerical and experimental determination of the onset yield surfaces is quite accurate for CuAlBe, CuAlZn, and CuAlNi, but is not accurate for NiTi. Sadjadpour [53] examined the constitutive response in terms of the set of admissible transformation strains. The key idea was to simplify the micromechanical considerations by treating the transformation strain as an ensemble average of all of the variants appearing in the microstructured sample. The definition of the set of transformation strains is the convex dual of the onset stress surface incorporated by Auricchio and LExcellent in their models. LExcellent and Laydi [40] examine this duality in detail. They describe the surface transport between stress and strain spaces as well as the convexity conditions for the class of surfaces they derived previously. It is important to notice that

these single-surface models are not panacea. In each of the cases mentioned above, the determination of the yield surfaces and their duals is accomplished through the fitting of many uniaxial data points. This is natural as the definition of the yield surface must have an associated normality rule. The downside of this in the polycrystalline case is that the polycrystal is replaced effectively with a single crystal. Many of the important experimental observations in polycrystals cannot be incorporated in this way. In particular, martensite reorientation and transformation saturation are not incorporated in these models.

Some polycrystalline models attempt to reproduce the important characteristics that are not accounted for in the yield surface models. Thamburaja and Anand [64] model the polycrystalline sample by incorporating a single-crystal model on the grain scale in a finite-element mesh. This model is able to capture the effects of texture on several different types of load cycle. It is very computationally demanding as the constitutive modelling is done on the level of the grain as opposed to true polycrystalline constitutive modelling. The computational model of Patoor et al. [47] incorporates the grain structure of the sample through Eshelby solutions that are ensemble averaged across the grains to determine a quadratic form for the energy associated with the transformation strain. The modelling approach of Brinson and her collaborators, that saw a good deal of success in the single crystal through the incorporation of self-accommodating groups of martensite variants, was extended to the polycrystal. Brinson and Panico [18] are able to capture the martensitic reorientation in three-dimensional polycrystals. The transformation strains associated with each variant are tracked as internal variables as well as the strains associated with the possible pairs of twinned martensitic variants in the polycrystal. Tracking this (possibly large) roster of internal variables and the associated driving forces allows for the microstructure in the sample to change during the loading cycle. This

innovation shows one way of incorporating the heretofore elusive phenomenon of martensitic reorientation.

2.2 Motivation

The objective of this thesis is to develop a constitutive relation for shape-memory alloys that is simple and robust, but also capable of describing diverse phenomena under complex thermomechanical loading so that it can be an effective tool in engineering analysis and design.

The key heuristic and the point of departure of this work is the recognition that the mechanics of initiation and saturation of the martensitic transformation in polycrystals are two essentially different processes. Consider a polycrystal completely in the austenite state above its transformation temperature, and subject it to an increasing stress. The *initiation* of transformation is governed by those grains that are best oriented to the applied load. In particular, Brinson et al. [19] used in-situ optical microscopy to observe that the first appearance of the martensite occurs in the form of isolated regions in well-oriented grains. This is supported by the mesoscale observations of Daly et al. [26] that deviations in linearity of the stress-strain curve occurs well before the formation of macroscopic transformed regions. Finally, Schlömerkemper and Bhattacharya [16] have recently proved in an idealized setting with uniform modulus that the transformation begins in isolated grains, and consequently the Sachs or Reuss constant stress bound accurately describes the initiation of the transformation. Thus, the essential mechanics of initiation is described by treating the grains as essentially non interacting, isolated bodies in the elastic austenite.

As the best oriented grains begin to transform, the grain boundary interactions

begin to increase in importance. The transformed regions lead to inhomogeneous stress and this in turn causes other grains to transform. Gradually the driving force is large enough for the poorly oriented grains to start transforming as well. However, they have smaller transformation strain in the direction of loading, and thus they begin to quickly saturate and "lock" together eventually leading to a network of fully transformed grains. Thus, the *saturation* of the transformation is governed by the poorly oriented grains. Indeed, Brinson et al. [19] observed substantial regions of untransformed austenite even when the macroscopic stress-strain curve had turned around to indicate macroscopic saturation of the transformation. Further, various theoretical and computational analysis have shown that the constant strain Taylor or Voigt bound gives a good description of the overall effective strains. [13, 58, 62]. Thus, the essential physics of saturation is described by looking at the poorly oriented grains, and one has retained austenite when the transformation has macroscopically saturated.

Finally, an important implication of the fact that the initiation and saturation of the martensitic transformation in polycrystals are two essentially different processes is that the critically resolved shear stress criterion or the Clausius-Clapeyron relation fails in a polycrystal (see [26]), though it is known to hold well in a single crystal (for example, [57]).

The discussion above has focussed on stress-induced transformation. The situation is slightly different in thermally induced martensite. Consider a polycrystal completely in the austenite state above the transformation temperature . As it is cooled, it transforms to martensite with two characteristic features. First, it is self-accommodating so that there is no macroscopic change in shape. In other words, even though individual unit cells change shape as a result of the transformation, the grains form such a microstructure of the different variant that there is no macroscopic

change in shape. Second, the transformation proceeds to completion. In other words, there is no retained austenite. Now deform this self-accommodated martensite. The microstructure changes to the extent it can under intergranular constraints to accommodate the applied load. However, as before, this deformation is constrained by a network of poorly oriented grains. Consequently the constant strain Taylor or Voigt bound gives a good description of the available strain through martensitic reorientation [13, 58, 62]. Finally, when the polycrystal in the deformed state is heated, it transforms back to the austenite accompanied with strain recovery.

Chapter 3

Continuum Model

3.1 Kinematics

We seek to incorporate the heuristics described in section 2.2 into a continuum model. We do so taking a multi scale view so that each material point of our continuum corresponds to a representative volume of material with numerous grains with possible fine-scale microstructure in each grain. We denote the strain as ε and the temperature as θ .

We then introduce two key kinematic or internal variables to incorporate the heuristic considerations described above. The first is the volume fraction λ of the martensite. The second is the *nominal transformation strain* of the martensite ε_m which we define as follows. Consider the representative volume that is partially transformed and average the transformation strain of every region of martensite in every grain in this representative volume. This is the nominal transformation strain. Note that this is not the overall or *effective transformation strain* which is given by $\lambda\varepsilon_m$. We refer the reader to Sadjadpour [53] for a detailed discussion of these variables.

These kinematic variables are subject to some constraints. The constraint on λ

is obvious:

$$\lambda \in [0, 1]. \quad (3.1)$$

The constraint on the nominal transformation strains is also relatively simple: it has to be a possible average of microstructures of martensite average over grains:

$$\varepsilon_m \in \mathcal{G}_i := \left\{ \xi : \xi = \sum_{i,n} \mu_{i,n} Q_n^T \varepsilon_i Q_n, \mu_{i,n} \geq 0, \sum_{i,n} \mu_{i,n} = 1 \right\} \quad (3.2)$$

where $\mu_{i,n}$ may be the volume fraction of the i th variant of martensite in the n th grain and Q_n is the rotation that describes the crystallographic orientation of the n th grain. We call the set \mathcal{G}_i the set of nominal transformation strains. Notice that this set considers all possible arrangements of martensite with no regard to compatibility. Therefore this set will play an important role when we consider initiation of transformation. Finally consider the constraint on the effective transformation strain: we require it be a value that one can obtain by making a kinematically compatible microstructure of martensite:

$$\lambda \varepsilon_m \in \mathcal{G}_s := \{ \xi : \xi = \text{average strain of a compatible microstructure of martensite.} \} \quad (3.3)$$

We call the set \mathcal{G}_s the set of effective transformation strains. It is identical to the set of recoverable strains defined by Bhattacharya and Kohn [13]. Notice that this set limits itself to compatible microstructures and thus is limited by networks of poorly oriented grains. Therefore this set will play an important role when we consider saturation of the transformation. From the definitions it is clear that the set of nominal

transformation strains is larger than the set of effective transformation strains:

$$\mathcal{G}_i \supset \mathcal{G}_s. \quad (3.4)$$

Before we proceed, it is instructive to look at these constraints in a one-dimensional situation. Here, ε_m is a scalar and the sets \mathcal{G}_i and \mathcal{G}_s are nested intervals:

$$\mathcal{G}_{i,s} = [\varepsilon_{i,s}^c, \varepsilon_{i,s}^t], \quad \varepsilon_i^c \leq \varepsilon_s^c \leq 0 \leq \varepsilon_s^t \leq \varepsilon_i^t. \quad (3.5)$$

The three constraints are plotted in figure 3.1, Note that when the material is in the austenite and $\lambda = 0$, ε_m can explore the entire interval \mathcal{G}_i . This is consistent with the physics that the initiation of stress-induced transformation is controlled by the best oriented grains. However, when the material is in the martensite and $\lambda = 1$, it can explore only a smaller interval \mathcal{G}_s because of the constraint on the effective transformation strain $\lambda\varepsilon_m$. This is consistent with the observation that the deformation of the thermally induced martensite is constrained by the compatibility of the grains. Similarly, note that the volume fraction can range from zero to one when we have a self-accommodated martensite ($\varepsilon_m = 0$) as during cooling. However, it can only explore a smaller region when ε_m is large as in the stress-induced situation.

3.2 Balance Laws

We postulate the usual balance laws of continuum mechanics. In local form, the balance of linear momentum and energy may be stated as

$$\rho u_{tt} = \operatorname{div} \sigma, \quad (3.6)$$

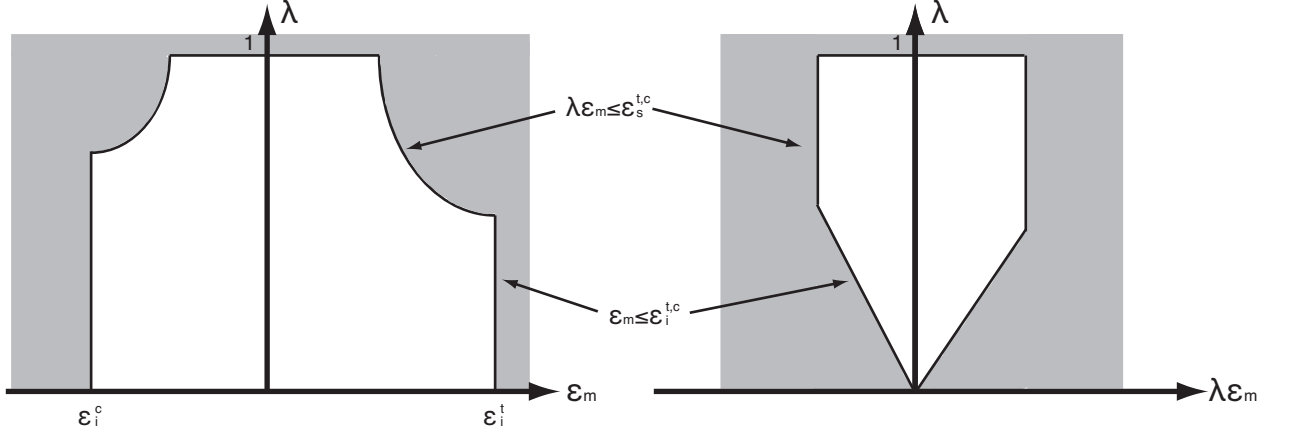


Figure 3.1: The volume fraction and the nominal effective strain are constrained to lie in the identified set.

$$\dot{\epsilon} = -\nabla q + r + \sigma : \dot{\epsilon}, \quad (3.7)$$

where u is the displacement, ρ is the (referential) mass per unit length, σ is the stress, ϵ is the internal energy density, q the heat flux and r the radiative heating. We also use the local form of the second law of thermodynamics,

$$-\dot{W} - \eta \dot{\theta} + \sigma : \dot{\epsilon} - \frac{q \nabla \theta}{\theta} \geq 0, \quad (3.8)$$

where $W = \epsilon - \theta \eta$ is the Helmholtz free energy density, η the entropy density and θ the (absolute) temperature.

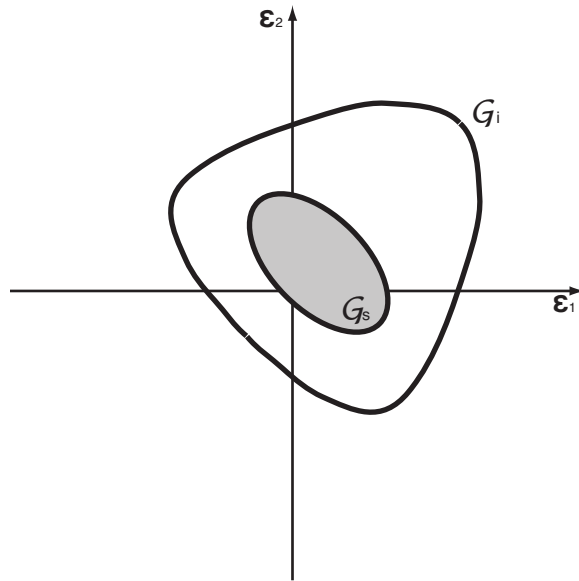


Figure 3.2: A schematic representation of sets $\mathcal{G}_{i,s}$

3.3 Energy

We assume that the Helmholtz free energy density of the system is given by

$$\begin{aligned}
 W(\varepsilon, \varepsilon_m, \lambda, \theta) &= \frac{1}{2}(\varepsilon - \lambda\varepsilon_m) : C(\varepsilon - \lambda\varepsilon_m) \\
 &\quad + \lambda\omega(\theta) - c_p\theta \ln\left(\frac{\theta}{\theta_0}\right) \\
 &\quad + G_i(\varepsilon_m) + G_s(\lambda\varepsilon_m).
 \end{aligned} \tag{3.9}$$

The first term on the right hand side is the elastic energy density. Here it is assumed that the total strain ε is the summation of the elastic component and the effective transformation strain $\lambda\varepsilon_m$. The material is assumed to have a constant elastic modulus tensor C in both phases for the sake of simplicity. To make the modulus a function of phase fraction would not unduly complicate matters. A simple $C(\lambda)$ could be chosen by simply taking a weighted average of the austenite and martensite moduli as the phase fraction varies from 0 to 1. Another, more exotic variation of the modulus tensor with the martensitic phase fraction can be chosen. As long as it is monotone, it should not change the tenor of the calculations to be undertaken.

The second term in the energy represents the change in chemical energy density between the austenite and martensite phase at the given transformation temperature, and can be written in the form

$$\omega(\theta) = \mathcal{L} \frac{(\theta - \theta_c)}{\theta_c},$$

where \mathcal{L} is the latent heat of transformation and θ_c is the thermodynamic transformation temperature (where the austenite and martensite phases are equally stable). The third term is the contribution of heat capacity and c_p is the specific heat which

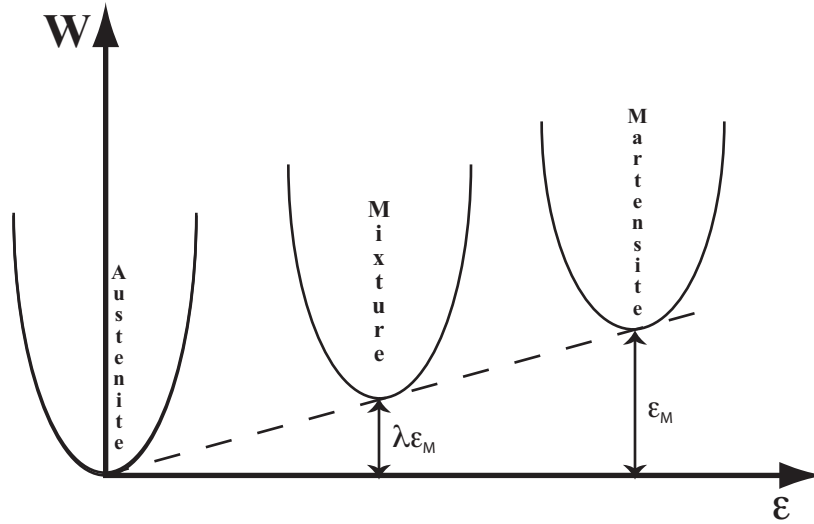


Figure 3.3: A schematic representation of the first two terms of W

is assumed to be equal in both the austenite and the martensite.

Finally the last two terms in the energy describe the increased energy with increasing transformation strain due to inhomogeneous stresses and also enforce the constraints (3.1), (3.2), and (3.3). We discuss these presently.

3.4 Initiation and Saturation

We postulate that the energy contributions G_i and G_s simply enforce the constraints and consequently have the simple form:

$$G_{i,s}(\xi) = \begin{cases} 0 & \xi \in \mathcal{G}_{i,s}, \\ +\infty & \text{else,} \end{cases} \quad (3.10)$$

where

$$\mathcal{G}_{i,s} = \left\{ \xi : \text{tr } \xi = 0 \text{ and } \frac{2}{3}(\xi \cdot \xi)^{3/2} + b_{i,s} \det(\xi) + \frac{1}{3}c_{i,s} |e_{i,s} \cdot \xi e_{i,s}|^3 - g_{i,s} \leq 0 \right\}, \quad (3.11)$$

and $b_{i,s}$, $c_{i,s}$, $g_{i,s}$ are material parameters. Here, we assume that the material is transversely isotropic about a direction \hat{e} . Therefore, the set can be described as a function of the three principle invariants of ξ and the elongation along \hat{e} . However, we have assumed self-accommodation so that the trace of all transformation strains are zero. Thus, the set can be described as functions of $|\xi|^2$, $\det \xi$ and $\hat{e} \cdot \xi \hat{e}$. We choose the form above for ease and to have uniform powers of ξ .

The effect of the three parameters is as follows: $g_{i,s}$ determines the size of the initiation and saturation surfaces respectively, $b_{i,s}$ determines the degree of tension compression asymmetry in the sample response due to the determinant term (figure 3.4), and $c_{i,s}$ imbues the specimen with a degree of uniaxial eccentricity in the direction $\hat{e}_{i,s}$ (figures 3.5 and 3.6).

It is worth noting that the uniaxial eccentricities varied through the terms c_i and c_s are certainly not the only anisotropies that could be feasibly incorporated into this model. In theory the only restrictions imposed on the sets \mathcal{G}_i and \mathcal{G}_s are those of convexity and energetic frame indifference. The intent of the uniaxial eccentricity

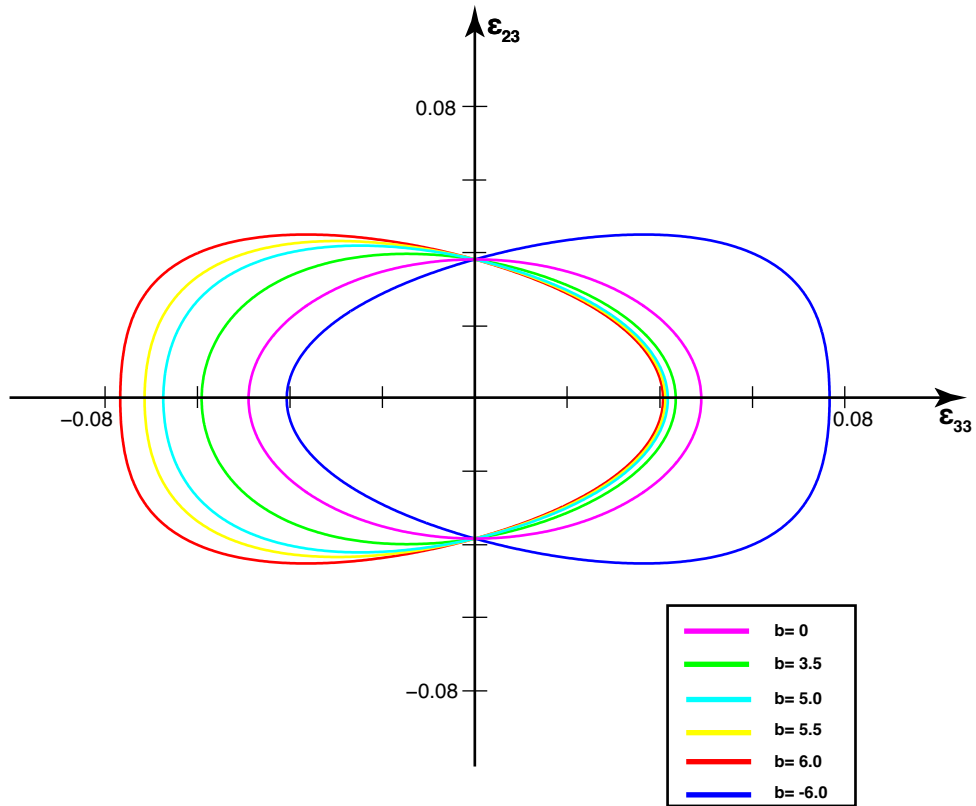


Figure 3.4: The degree of tension-compression asymmetry of the initiation and saturation surfaces is adjusted through the parameter b .

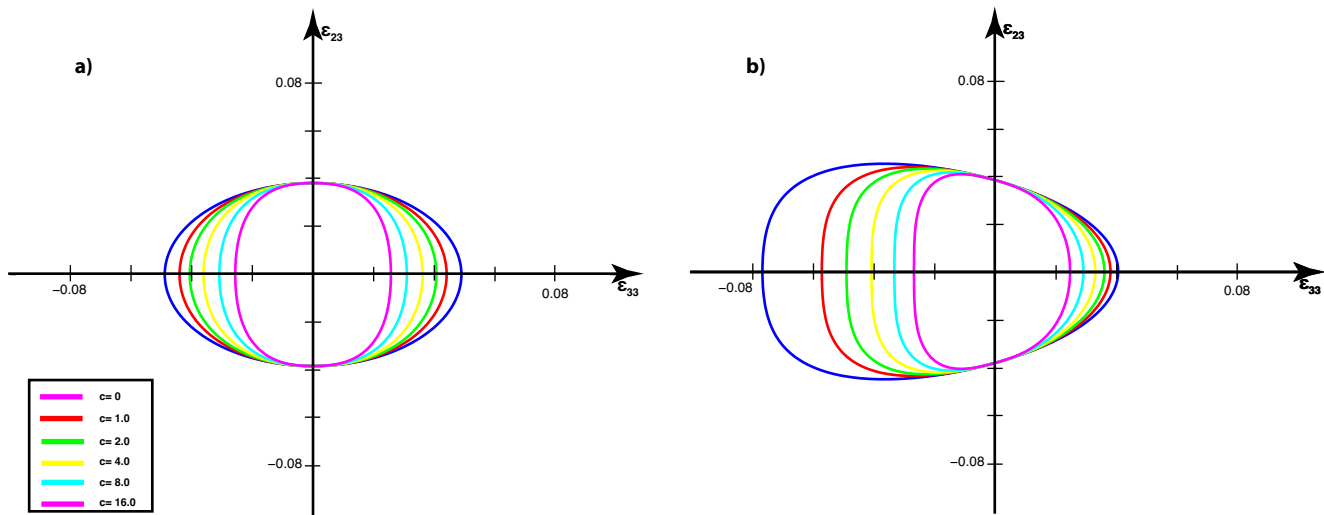


Figure 3.5: The degree of eccentricity of the initiation and saturation surfaces is varied through the parameter c . The effects of variation of this parameter are seen on a) a symmetric set, and b) a set with a high degree of asymmetry.

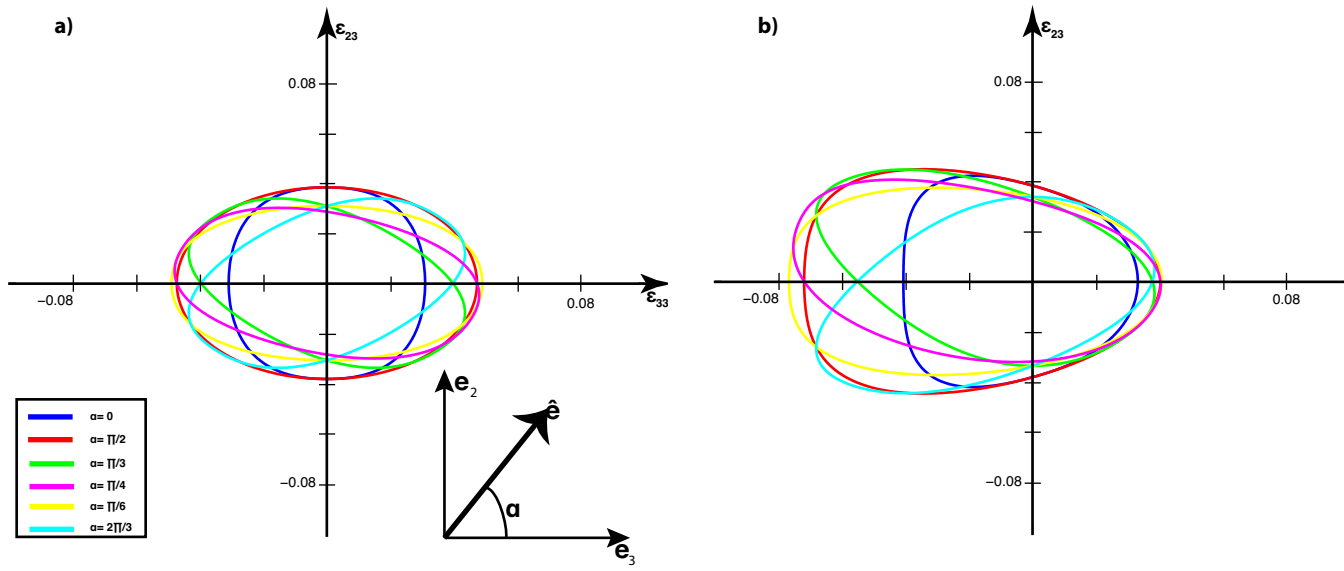


Figure 3.6: The direction of eccentricity is controlled through variation of the vector \hat{e} . The effects of variation of this parameter are seen on a) a symmetric set, and b) a set with a high degree of asymmetry.

is merely to account for circumstances, such as those previously mentioned experiments on the effect of rolling direction on the response of thin sheets of NiTi, which introduce a highly directional anisotropy in the material response.

The proposed functions for \mathcal{G}_i and \mathcal{G}_s are intentionally simple in their formulation. In general, taken as they are, these functions may not be sufficient to fit a given set of experiments. However, they should be able to incorporate the striking experimental phenomena of tension-compression asymmetry and directional anisotropy. An important example of this is in the isotropic but asymmetrical experiments of LExcellent et al. [39]. The surface of transformation onset stresses is determined experimentally in the case of biaxial tension and compression. As the investigators state, a yield surface that is a level set of the type of function that has been proposed (a linear combination of norm and determinant terms) is inadequate to fit the given experiments. They propose a surface of the type:

$$\mathcal{F}(y) = \left\{ \cos \left(\frac{\arccos(1 - a(1 - y))}{3} \right) \leq f \right\}, \quad (3.12)$$

with $a \in (-1,1)$ and y related to the determinant of the deviatoric stress.

$$y = \frac{27}{2} \frac{\det(\text{dev}\sigma)}{\left(\frac{3}{2}\text{dev}\sigma : \text{dev}\sigma\right)^{\frac{3}{2}}}. \quad (3.13)$$

The distinction is drawn between the stress yield surface $\mathcal{F}(\sigma)$ and its convex dual $\mathcal{G}_i(\varepsilon_M)$ that is of interest to this model. On first observation it seems clear that the dual of the type of surface described in 3.12 cannot be generally fit by those described in 3.11. With a suitable choice of parameters, the general shape can be recovered.

Quantitatively the experimental data could, of course, be fitted in a least squares manner. A more convenient choice is to select those values for the parameters b_i

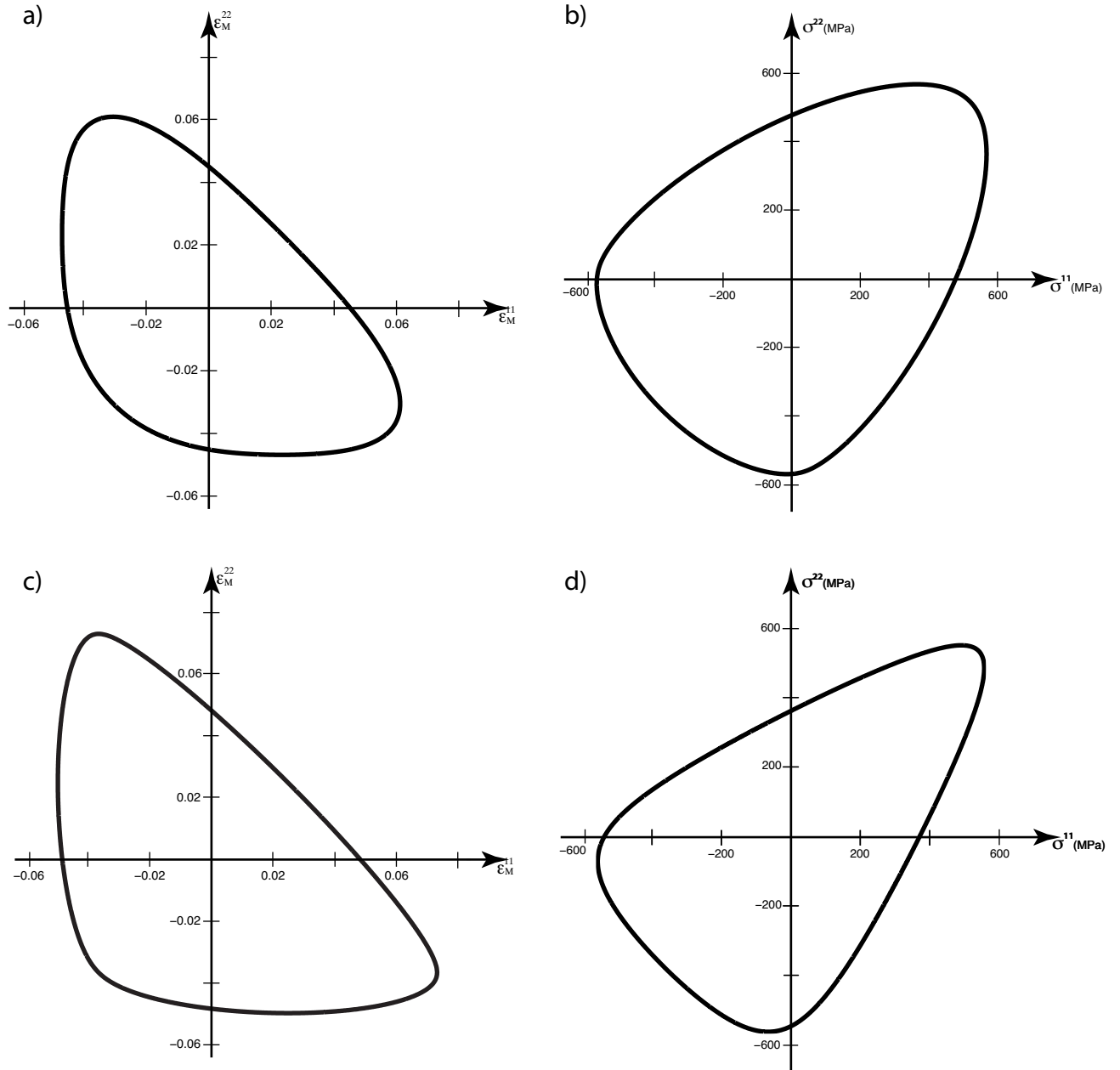


Figure 3.7: A suitable choice of parameters for the set of admissible transformation strains (a) allows for recovery of the tension-compression asymmetry in the biaxial experiments in the dual stress space (b). A more precise fit to the experimental data was proposed by Lexcellent in d) and its strain-space dual in c).

and g_i which allows for the incorporation of the key phenomenon presented. In this case, since in the sequel we are concerned with tension-compression and tension-shear tests, the choices of b_i and g_i are made to recover the tension-compression asymmetry of the experiments. In figure 3.7 the parameters are set to $b_i = -1.85$ and $g_i = 2.05 \times 10^{-4}$ in order to meet this end. It is worth noting that the proposed $\mathcal{F}(\sigma)$ is convex (and so must be its dual) and frame indifferent. It could be incorporated into the model. This would be an excellent course of action if the biaxial load case was the specific point of investigation of this thesis. The mathematical complexity that this would add to the formulation might prove more cumbersome than it is worth in a general investigation of how the nature of initiation and saturation surfaces effect the macroscopic response of the alloy.

3.5 Driving Forces and Kinetics

With the free energy density specified, we can use the dissipation inequality and arguments following Coleman and Noll [25] to obtain constitutive relations for the stress and entropy:

$$\sigma = C(\varepsilon - \lambda \varepsilon_m), \quad (3.14)$$

$$\eta = \lambda \frac{\mathcal{L}}{\theta_{cr}} - c_p \left(1 + \ln \left(\frac{\theta}{\theta_0} \right) \right). \quad (3.15)$$

We also obtain the following driving forces as the thermodynamic conjugates to the internal variables λ and ε_m respectively:

$$\begin{aligned} d_\lambda &= -\frac{\partial W}{\partial \lambda} \\ &= (\varepsilon - \lambda \varepsilon_M) : (C) \varepsilon_M - \omega(\theta) - \frac{\partial G_s}{\partial (\lambda \varepsilon_M)} : \varepsilon_M \end{aligned} \quad (3.16)$$

$$\begin{aligned}
&= \sigma : \varepsilon_M - \omega(\theta) - \frac{\partial G_s}{\partial(\lambda \varepsilon_M)} : \varepsilon_M, \\
d_{\varepsilon_m} &= -\frac{\partial W}{\partial \varepsilon_M} \\
&= \lambda C(\varepsilon - \lambda \varepsilon_M) - \frac{\partial G_i}{\partial \varepsilon_M} - \lambda \frac{\partial G_s}{\partial(\lambda \varepsilon_M)} \\
&= \lambda \sigma - \frac{\partial G_i}{\partial \varepsilon_M} - \lambda \frac{\partial G_s}{\partial(\lambda \varepsilon_M)}.
\end{aligned} \tag{3.17}$$

In writing these relations, we have assumed that the functions $G_{i,s}$ are smooth. In the non-smooth situation (i.e., in the case in which the energies $G_{i,s}$ are zero-infinity wells), the differentiation that must be done in order to find the driving forces is slightly more subtle. The tensorial derivatives $\frac{\partial G_i}{\partial \varepsilon_M}$ and $\frac{\partial G_s}{\partial(\lambda \varepsilon_M)}$ must be understood as subdifferentials, $\partial_{\varepsilon_M} G_i$ and $\partial_{\lambda \varepsilon_M} G_s$. This is a classical idea in the literature of convex analysis (see for example [51]). Inside the set \mathcal{G} , the subdifferential is identically 0. On the boundary of \mathcal{G} the subdifferential is multivalued (i.e., consisting of multiple subgradients). The directional derivative of the constraint energy G on the boundary of \mathcal{G} is defined by the supremum:

$$G'(\varepsilon; \delta x) = \sup_{g \in \partial G(\varepsilon)} g : \delta x. \tag{3.18}$$

This convex program can be incorporated into a descent algorithm to minimize the proposed energy numerically. However this can be an onerous process, amounting to numerically solving constrained minimization problems with Lagrange multipliers. Minimization is made much easier by a smoothing of the constraint energies. The particular form of smoothing used in simulations is discussed in a later chapter.

We are now in a position to specify the evolution laws, or kinetic relations, for our internal variables λ and ε_M . We assume that the martensitic variants can rearrange

much more easily than the phase transformation can proceed, and thus ε_M has much faster kinetics than λ . In fact, we take this to an extreme and insist on equilibrating ε_M at each time. In the non-smooth case this reduces to:

$$\varepsilon_M = \max_{\varepsilon_M \in \partial(\mathcal{G}_i \cap \lambda \mathcal{G}_s)} \sigma : \varepsilon_M. \quad (3.19)$$

We assume that the phase transformation evolves according to the kinetic relation:

i) Stick-Slip

$$\dot{\lambda} = \begin{cases} \dot{\lambda}^+ \left(1 + \frac{1}{(d_\lambda - d_\lambda^+)}\right)^{\frac{-1}{p}} & d_\lambda \geq d_\lambda^+ \text{ and } \lambda \leq 1 \\ \dot{\lambda}^- \left(1 + \frac{1}{(d_\lambda^- - d_\lambda)}\right)^{\frac{-1}{p}} & d_\lambda \leq d_\lambda^- \text{ and } \lambda \geq 0 \\ 0 & \text{else.} \end{cases} \quad (3.20)$$

ii) Rate Independent Kinetics

$$\dot{\lambda} = \begin{cases} +\infty & d_\lambda \geq d_\lambda^+ \text{ and } \lambda \leq 0 \\ -\infty & d_\lambda \leq d_\lambda^- \text{ and } \lambda \geq 0 \\ 0 & \text{else.} \end{cases} \quad (3.21)$$

The rate-independent kinetic law reduces to a simultaneous equilibration of the variables λ and ε_M . When the driving force ($\sigma : \varepsilon_M - \omega(\theta)$) remains in $(d_\lambda^-, d_\lambda^+)$ no change in λ occurs. When the driving force threshold is exceeded, the new value of λ can be determined in the non-smooth case by finding the equilibrium value of ε_M

for each value of λ as in 3.19. The equilibrium equation for λ is given by:

$$\lambda = \min_{\sigma:\varepsilon(\lambda)-\omega(\theta)\in(d_\lambda^-,d_\lambda^+)} |\lambda - \lambda_0|. \quad (3.22)$$

It is important that the kinetic relation chosen incorporates some characteristics observed in the experimental literature and the theory. Shaw and Kyriakides [56] observed the stick-slip behavior of the martensite transformation. The growth of bands of martensite was triggered when a critical tensile stress was exceeded and stopped when the stress was relaxed below that level. Careful investigation of the hysteresis associated with these transformation processes [7] showed that the energy under the hysteresis loop did not change depending on the rate at which loading and unloading occurred. Traditionally, many microscopic models of phase transformations are modeled with viscous kinetics which are linear near zero driving force. Chu, James and Abeyaratne [2] and Bhattacharya [11] were able to reconcile the discrepancy between the microscopically viscous kinetics and the stick-slip, rate-independent behavior observed macroscopically. The defects present in a "wiggly" energy landscape were shown to locally arrest phase-boundary motion. The effect of this local pinning on the microscopic viscous kinetics on the whole was a rate-independent stick-slip kinetics. Dondl [28] extended this work to two-dimensional systems. Stick-slip behavior is incorporated in both kinetic laws through the condition $\dot{\lambda} = 0$ for $d_\lambda \in (d_\lambda^-, d_\lambda^+)$. The rate independence, the indeterminate transformation speed when the critical driving force is exceeded, is incorporated by requiring a vertical tangent in both curves at the critical driving force.

The important difference between the two kinetic laws is in the regime of high driving forces. The rate-independent model makes the simplifying assumption that the phase fraction of martensite equilibrates essentially infinitely quickly. The stick-

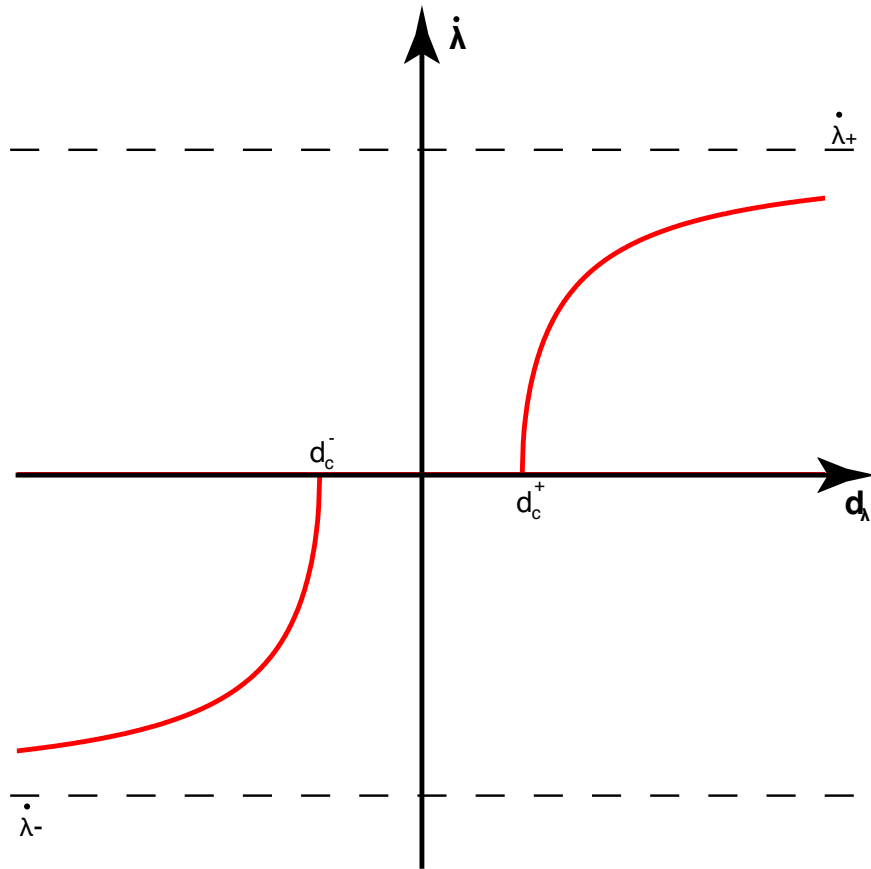


Figure 3.8: The kinetic relation governing the phase transition in the stick-slip case.

slip condition makes an assumption, slightly more appealing to common sense, that in the limit of high driving forces the rate of transformation must approach a limiting speed asymptotically. This assumption of limiting speed, ostensibly the sound speed of the material, follows the work of Purohit [50] for example. It is important to note that the rationale for this assumption is a dynamic one. The setting of this problem is quasistatic. Derivation of kinetic relations in the dynamic setting is still largely an open issue.

Chapter 4

Some Features of the Model

We now demonstrate a few features of the model.

4.1 One Dimension

We specialize the model to one dimension so that

$$W(\varepsilon, \varepsilon_m, \lambda, \theta) = \frac{1}{2}C |\varepsilon - \lambda\varepsilon_m|^2 + \lambda\omega(\theta) - c_p\theta \ln\left(\frac{\theta}{\theta_0}\right) + G_i(\varepsilon_m) + G_s(\lambda\varepsilon_m), \quad (4.1)$$

where the sets $\mathcal{G}_{i,s}$ are given by (3.5). We further assume that kinetics of ε_m is extremely fast so that it minimizes the energy at each instant of time and that λ follows a strict rate-independent stick-slip kinetics:

$$\dot{\lambda} = 0 \text{ for } d_\lambda \in (d_\lambda^-, d_\lambda^+), \quad d_\lambda \in [d_\lambda^-, d_\lambda^+], \quad d_\lambda \dot{\lambda} \geq 0. \quad (4.2)$$

4.1.1 Stress-Induced Martensite

Consider an isothermal strain-controlled experiment where the temperature is held constant at a value significantly higher than the transformation temperature so that

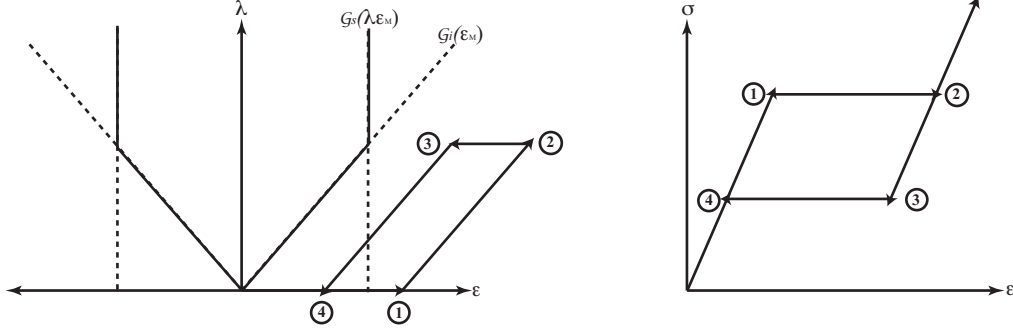


Figure 4.1: Stress-induced martensite in one dimension shown in the volume fraction-strain plane on the left and the stress-strain plane on the right. The constraints on the volume fraction and nominal transformation strain are indicated on the shaded set.

$\omega(\theta) > -d_\lambda^- > 0$. Consider the specimen at rest at zero stress so that it is in the austenite state with $\lambda = 0$ and $\varepsilon_m \in [\varepsilon_i^c, \varepsilon_i^t]$ indeterminate. Now subject the specimen to a monotonically increasing overall strain tensile strain $\varepsilon(t)$. For very small times, the stress is given by $\sigma(t) = C\varepsilon(t)$. Since this is positive, the nominal transformation strain ε_m , takes its maximal tensile value ε_i^t and the driving force for transformation, $d_\lambda = \sigma\varepsilon_i^t - \omega$ is too small begin transformation (i.e., in the range $(d_\lambda^-, d_\lambda^+)$ so that $\dot{\lambda} = 0$). Thus the volume-fraction, stress and strain begin from zero and traverse toward the point marked 1 in figure 4.1.

As the applied strain increases, so do the stress and the driving force d_λ until we reach the point marked 1 in the figure where $d_\lambda = C\varepsilon - \omega = d_\lambda^+$ and transformation begins. At this point, the strain and stress are given as

$$\varepsilon_{MS}^t = \frac{d_\lambda^+ + \omega}{C\varepsilon_i^t}, \quad \sigma_{MS}^t = \frac{d_\lambda^+ + \omega}{\varepsilon_i^t}. \quad (4.3)$$

At this point transformation begins and proceeds in such a manner to keep d_λ and consequently the stress σ constant so that we traverse from the point marked 1

towards the point marked 2 in figure 4.1 as the applied load increases. As λ increases, the overall transformation strain $\lambda \varepsilon_m$ eventually saturates the constraint $\lambda \varepsilon_m \leq \varepsilon_s^t$ at the value

$$\lambda^t = \frac{\varepsilon_s^t}{\varepsilon_i^t}. \quad (4.4)$$

This is indicated by the point 2 in the figure, and we have

$$\varepsilon_{MF}^t = \frac{d_\lambda^+ + \omega}{C\varepsilon_i^t} + \varepsilon_s^t, \quad \sigma_{MF}^t = \frac{d_\lambda^+ + \omega}{\varepsilon_i^t}. \quad (4.5)$$

The transformation is now saturated, and further loading does not further lead to any further transformation. Thus, the stress increases linearly to the applied strain as indicated by the increasing branch of the stress-strain curve in figure 4.1.

Now start unloading the specimen by monotonically decreasing the applied tensile strain. There is no transformation initially and we unload elastically (the stress decreasing linearly with strain) until we reach the point marked 3 when the driving force has reached a low enough value to start reverse transformation, $d_\lambda = \sigma \varepsilon_i^t - \omega = d_\lambda^-$ so that

$$\varepsilon_{AS}^t = \frac{d_\lambda^- + \omega}{C\varepsilon_i^t} + \varepsilon_s^t, \quad \sigma_{AS}^t = \frac{d_\lambda^- + \omega}{\varepsilon_i^t}. \quad (4.6)$$

Reverse transformation now begins as λ begins to decrease as unloading proceeds. The driving force and stress remain constant and we traverse from point 3 to point 4 on figure 4.1. The reverse transformation is complete at the point 4 when $\lambda = 0$, and

$$\varepsilon_{AF}^t = \frac{d_\lambda^- + \omega}{C\varepsilon_i^t}, \quad \sigma_{AF}^t = \frac{d_\lambda^- + \omega}{\varepsilon_i^t}. \quad (4.7)$$

The material responds elastically on further unloading and we return to the origin.

We have an analogous situation in a compressive loading cycle with the analogous quantities obtained by replacing the superscript t with c in the formulae (4.3) to (4.7)

above.

A series of comments are in order. First, note that the transformation from austenite to martensite does not go to completion at a maximum volume fraction of $\lambda^{t,c}$. This is consistent with the observations of Brinson et al. [19].

Second, tension and compression are different. This is consistent with various observations going back to Burkart and Read [22].

Third, the value of stress at which the transformation begins and completes or the reverse transformation begins and completes depend on temperature through ω . If ω depends linearly in temperature as in most common models $\omega = L(\theta - \theta_c)$ where L is the latent heat, then these stresses depend linearly on temperature consistent with the Clausius-Clapeyron relation in a particular deformation mode. Further, we can invert these relations to obtain the values of temperature where the transformation begins etc at zero stress:

$$M_s = M_f = \theta_c - \frac{d_\lambda^+}{L}, \quad A_s = A_f = \theta_c + \frac{d_\lambda^-}{L}. \quad (4.8)$$

Fourth we can infer the values of transformation strain, the stress hysteresis and mean-value of stress in the hysteresis to be

$$\varepsilon_{trans}^{t,c} := \frac{1}{2}(\varepsilon_{MF}^{t,c} - \varepsilon_{MS}^{t,c} + \varepsilon_{AS}^{t,c} - \varepsilon_{AF}^{t,c}) = \varepsilon_s^{t,c}, \quad (4.9)$$

$$\sigma_{hyst}^{t,c} := \frac{1}{2}(\sigma_{MS}^{t,c} + \sigma_{MF}^{t,c} - \sigma_{AF}^{t,c} - \sigma_{AS}^{t,c}) = \frac{d_\lambda^+ - d_\lambda^-}{\varepsilon_i^{t,c}}, \quad (4.10)$$

$$\bar{\sigma}^{t,c} := \frac{1}{4}(\sigma_{MS}^{t,c} + \sigma_{MF}^{t,c} + \sigma_{AF}^{t,c} + \sigma_{AS}^{t,c}) = \frac{1}{2} \frac{d_\lambda^+ + d_\lambda^- + 2\omega}{\varepsilon_i^{t,c}}. \quad (4.11)$$

Note that each of them can be independently constitutively prescribed and that there is no universal relation amongst them. This is a manifestation of the lack

of any "resolved stress" criterion or Clausius-Clapeyron relation across deformation modes.

Fifth, we see above that $\sigma_{MS}^{t,c} = \sigma_{MF}^{t,c}$, $\sigma_{AS}^{t,c} = \sigma_{AF}^{t,c}$ and $M_s = M_f$. These are all manifestations of i) rate-independent or strictly stick-slip kinetics (3.21) and ii) isothermal conditions. If we assume that the material has a rate-dependent kinetic relation as in (3.20), then we would have $\sigma_{MF}^t > \sigma_{MS}^t$ with the difference depending on the loading rate. We would also have these if we assume non-isothermal situation. To elaborate on this, let us assume rate-independent kinetics and adiabatic conditions. Then, we have to solve (3.7) with $q = r = 0$. If we further assume that $\omega = L(\theta - \theta_c)$, we can show that the contribution of the latent heat to the driving force will require an increase in stress to sustain and saturate the martensitic transformation. Recall that

$$d_\lambda = \sigma : \varepsilon_i^{t,c} - \omega = \sigma : \varepsilon_i^{t,c} - L(\theta - \theta_c). \quad (4.12)$$

In order to initiate transformation, the driving force d_λ must equal the critical driving force d_λ^+ . The stress required to initiate transformation is written

$$\sigma_{MS} = \frac{d_\lambda^+}{\varepsilon_i^{t,c}} - \frac{L(\theta_0 - \theta_c)}{\varepsilon_i^{t,c}}. \quad (4.13)$$

In the isothermal case, the temperature remains constant at θ_0 throughout the transformation. In the adiabatic case, the constitutive assumption

$$c_p \dot{\theta} = \theta \dot{\lambda} L \quad (4.14)$$

must be integrated in order to yield the temperature change throughout the transformation process.

$$\theta(t) = \theta_0 \exp\left(\frac{L(\lambda(t) - \lambda(0))}{c_p}\right) \quad (4.15)$$

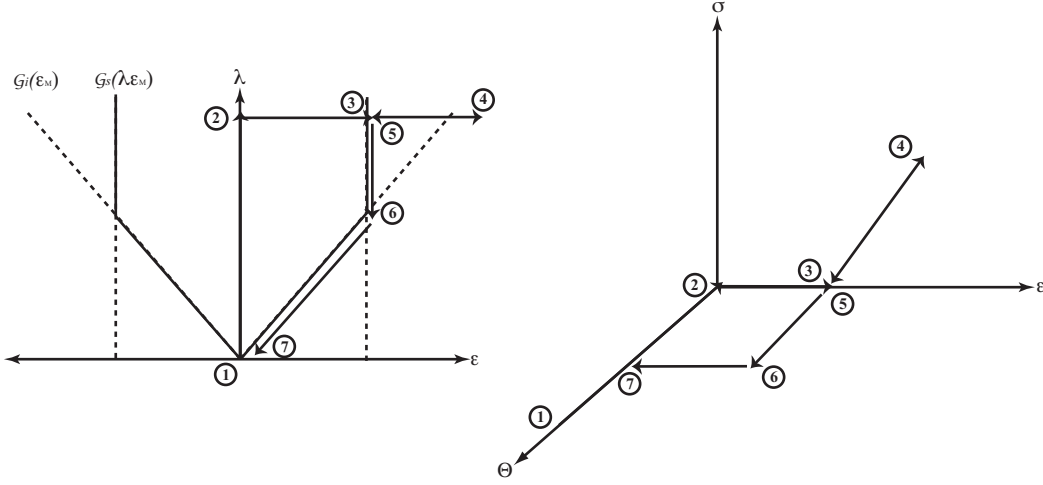


Figure 4.2: Shape-memory effect in one dimension shown in the the volume fraction-strain plane on the left and the stress-strain-temperature space on the right. The constraints on the volume fraction and nominal transformation strain are indicated on the shaded set.

The temperature at saturation is going to be $\theta_f = \theta_0 \exp\left(\frac{L\lambda_{sat}}{c_p}\right)$. Plugging this into the driving force equality yields the stress as the saturation of transformation

$$\sigma_{MF} = \frac{d_\lambda^+}{\varepsilon_i^{t,c}} - \frac{L(\theta_f - \theta_c)}{\varepsilon_i^{t,c}}, \quad (4.16)$$

$$\sigma_{MF} - \sigma_{MS} = \frac{L\theta_0}{\varepsilon_i^{t,c}} \left(\exp\left(\frac{L\lambda_{sat}}{c_p}\right) - 1 \right); \quad (4.17)$$

yields the extent of hardening in the adiabatic situation.

4.1.2 Shape-Memory Effect

We now subject our one dimensional specimen to a controlled (infinitely slow) temperature-load cycle to explore the shape-memory effect. We begin, as before with an unloaded

specimen at a temperature above A_f . This is marked as the point 1 in figure 4.2. We lower the temperature below M_s and M_f so that the material transforms to martensite and λ goes to 1 as we traverse from point 1 to point 2 in the figure. We now keep the temperature constant and subject the material to a strain controlled loading unloading cycle. The moment the strain and consequently the stress becomes positive, the nominal transformation strain ε_m takes the value ε_i^t to optimize the energy and we traverse from point 2 to point 3 in the figure. Now the overall strain is the transformation strain ε_s^t . Note that this happens at a value of stress equal to 0^+ since we assume that the kinetics of ε_m is infinitely fast. Further loading takes us to point 4, and unloading brings us to 5 (which coincides with 3 in the stress-strain-temperature space). We now keep the stress zero and heat the specimen. There is no change in strain or transformation and traverse from point 5 to point 6 (which coincide on the left) in the figure. At point 6, the temperature has reached A_s so that $d_\lambda = \omega = d_\lambda^-$, the reverse transformation begins and the volume fraction decreases. We traverse from point 6 to point 7 (which happen to coincide on the right) on the figure. As the volume fraction decreases at this fixed temperature, it eventually reaches the point λ^t at which point the constraint on the effective transformation strain is activated. Now, any further reduction in volume fraction can only occur with a reduction in ε_m and strain recovery. Therefore we traverse from point 6 to point 7 in the figure. Further heating brings us back to the starting point.

Note that in the thermal cycle, there is no restriction on the amount of transformation, and the specimen is able to transform fully to martensite. Once again, rate and heat transfer effects would make the curves rounded.

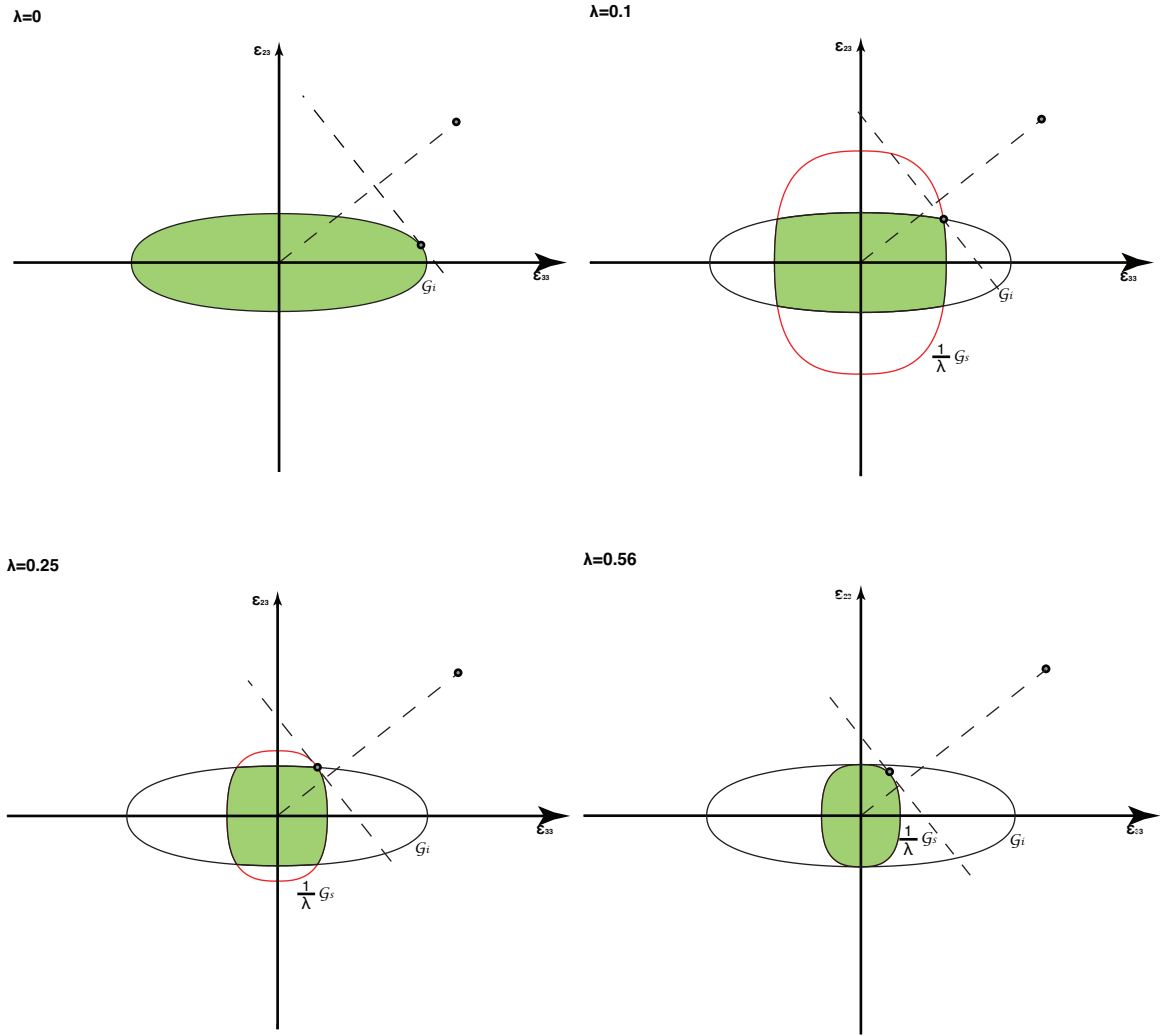


Figure 4.3: The different eccentricities of the set \mathcal{G}_i and \mathcal{G}_s can lead to a significant reorientation of the martensite. The nominal transformation strain at different extents of transformation is shown.

4.2 Martensite Reorientation

An important aspect of the interaction that we seek to incorporate in our model is the fact that initiation and saturation are controlled by different aspects in a polycrystal. Therefore it is possible for the martensite to reorient as the transformation proceeds, i.e., the variants and proportions that are present at initiation may be quite different from those present at saturation. We now demonstrate how this arises in our model as a result of different eccentricities of the sets \mathcal{G}_i and \mathcal{G}_s . We note that the sets \mathcal{G}_i and \mathcal{G}_s can have different eccentricities even when they have consistent material symmetry since the ratios of the parameters a_i, b_i, c_i can be different from those of a_s, b_s, c_s . Indeed, Schlömerkemper [54] has recently pointed out that the eccentricities of the Sachs and Taylor estimates of the set of recoverable strains of an isotropic polycrystal made of a material undergoing cubic-orthorhombic transformation can be quite different.

We now consider an idealized setting where the stress and strain are two dimensional vectors. We assume that the set \mathcal{G}_i is elongated along the $(\varepsilon_m)_1$ direction while the set \mathcal{G}_s is elongated in the $(\varepsilon_m)_2$ direction as noted in figure 4.3. We consider a situation when the crystal is above A_f , and subject it to a steady dead load in the direction σ sufficiently large to eventually initiate and saturate the transformation. As λ starts at zero and evolves until it eventually saturates at some value λ_{max} , the nominal transformation strain ε_m has to be optimized subject to the constraint that it is restricted to the set $\mathcal{G}_i \cap \frac{1}{\lambda}\mathcal{G}_s$. This is done by finding the point in the set $\mathcal{G}_i \cap \frac{1}{\lambda}\mathcal{G}_s$ that has a maximum projection in the direction σ . This is demonstrated in figure 4.3 for various values of λ . As λ changes, ε_m changes from a direction where it is optimized in \mathcal{G}_i to a direction where it is optimized in \mathcal{G}_s . Due to the fact that the initiation and saturation constraints have markedly different eccentricities, these di-

rections are quite different resulting a significant reorientation as the transformation proceeds.

Chapter 5

Demonstration and Parameter Study

We now turn to a systematic demonstration and parameter study of the model presented in chapter 3.

For the sake of consistency we specify a set of base parameters which shall be used in the absence of statements to the contrary. In order to replicate the tension-compression asymmetry seen in the onset surface of Lexcellent [41], mentioned previously, the initiation parameters are set as $b_i = -1.85$ and $g_i = 2.05 \times 10^{-4}$. No asymmetry is assumed in general for the saturation surface ($b_s = 0$). As the saturation surface must be contained within the initiation set, g_s is set to 2.25×10^{-5} . No anisotropy is assumed as a base for either surface. The Young's modulus is chosen as 115GPa.

For the thermal parameters we utilize the same base set as Sadjadpour [53]. The latent heat $L = 79 \left(\frac{MJ}{m^3}\right)$, the heat capacity $c_p = 5.4 \left(\frac{MJ}{m^3K}\right)$, the Martensite start $M_s = 217.60K$, and Austenite start $A_s = 266.79K$ are chosen as base parameters.

These are used to select the kinetic parameters.

$$d_\lambda^+ = -d_\lambda^- = L \left(\frac{A_s - M_s}{A_s + M_s} \right) = 8x10^6 \left(\frac{J}{m^3} \right) \quad (5.1)$$

Using the fact that the critical temperature, $\theta_{cr} = \frac{A_s + M_s}{2}$, the isothermal loading tests are conducted at a temperature chosen to make $\omega(\theta)$ a round number ($\theta = 333K$):

$$\omega(\theta) = \frac{L}{\theta_{cr}} (\theta - \theta_{cr}) = 1x10^7 \left(\frac{J}{m^3} \right). \quad (5.2)$$

Finally, the stick-slip exponent p is chosen to be 2.

It is assumed that the temperature is well above the transformation temperature.

In the absence of stress, the austenite is the stable phase.

This demonstration focuses on the interplay between the onset and saturation constraints. Particularly we are concerned with how the geometry of each constraint can give rise to some of the important features discussed in the previous chapter.

5.1 Uniaxial Tension and Compression

We consider the isotropic situation ($c_i = c_s = 0$) with strict rate-independent stick-slip kinetics (3.21) for the volume fraction. We consider a specimen well above transformation temperature so that $\lambda = 0$ and subject it to an uniaxial tension or compression. The resulting stress-strain curve is as shown on the right-hand side of figure 4.1 as we presently see. Assume that the applied load is along the e_3 axis so that the deviatoric stress is

$$\hat{\sigma} = \frac{\sigma}{3} \text{diag}\{-1, -1, 2\}.$$

As the load increases from zero, the nominal effective strain ε_m takes the value that optimizes its projection along the applied load ($\varepsilon_m : \hat{\sigma}$) amongst all allowable values in the set \mathcal{G}_i . Since we are in the isotropic case, symmetry dictates that the optimal strain will be of the form

$$\varepsilon_m = \frac{x}{3} \text{diag}\{-1, -1, 2\},$$

for some known x . Substituting this in the formula (3.11) for \mathcal{G}_i , we conclude that the optimal x satisfies,

$$\frac{2}{3} \left(\frac{2}{3} x_{t,c}^2 \right)^{\frac{3}{2}} \pm b_i \left(\frac{2}{27} x_{t,c}^3 \right) = g_i \implies x_{t,c} = \pm \left(\frac{g_i}{\left(\frac{2}{3} \right)^{\frac{5}{2}} \pm \frac{2}{27} b_i} \right)^{\frac{1}{3}}, \quad (5.3)$$

with the choice of positive sign for tension and negative for compression. We substitute this in the equation for the driving force, and find that the stress is initially too small to induce any transformation. So the material responds elastically. The transformation begins when the driving force it reaches its critical value d_λ^+ .

We conclude that transformation initiates at the following stress:

$$\sigma_{MS}^{t,c} = \pm \frac{3}{2} \left(\frac{\omega(\theta) + d_c^+}{g_i^{\frac{1}{3}}} \right) \left(\left(\frac{2}{3} \right)^{\frac{5}{2}} \pm \frac{2}{27} b_i \right)^{\frac{1}{3}}, \quad (5.4)$$

with the choice of positive sign for tension and negative for compression. Since the response is linear up to this point, the onset strain is obtained by dividing these with the Young's modulus. Since we have a strict rate-independent kinetics, the transformation proceeds at constant stress until we effective transformation strain saturates the constraint $\lambda \varepsilon_m \in \mathcal{G}_s$. This leads to equations similar to (5.3) with x replaced by λx , and b_i, g_i with b_s, g_s . We conclude that the saturation volume

fractions of the martensite are given by

$$\lambda_{sat}^{t,c} = \left(\frac{\left(\frac{2}{3}\right)^{\frac{5}{2}} \pm \frac{2}{27}b_i}{\left(\frac{2}{3}\right)^{\frac{5}{2}} \pm \frac{2}{27}b_s} \right)^{\frac{1}{3}} \left(\frac{g_s}{g_i} \right)^{\frac{1}{3}}, \quad (5.5)$$

with the choice of positive sign for tension and negative for compression. The associated transformation strain, the change in strain during the transformation, is given by

$$\varepsilon_{trans}^{t,c} = \left(\frac{g_s}{\left(\frac{2}{3}\right)^{\frac{5}{2}} \pm \frac{2}{27}b_s} \right)^{\frac{1}{3}}, \quad (5.6)$$

with the choice of positive sign for tension and negative for compression.

The transformation is now saturated. Thus, as the load increases the material responds elastically. Now start unloading. The driving force is too large to have any reverse transformation. The reverse transformation begins when the driving force reaches d_c^- and this corresponds to an applied stress of

$$\sigma_{AS}^{t,c} = \pm \frac{3}{2} \left(\frac{\omega(\theta) + d_c^-}{g_i^{\frac{1}{3}}} \right) \left(\left(\frac{2}{3}\right)^{\frac{5}{2}} \pm \frac{2}{27}b_i \right)^{\frac{1}{3}}, \quad (5.7)$$

with the choice of positive sign for tension and negative for compression. The volume fraction of martensite decreases at constant stress until it reaches zero, and the change in strain during this process is identical to transformation strain (5.6). As the load decreases further and to zero, the material unloads elastically to the origin.

Comparing (5.4) and (5.7), we find that the stress hysteresis during this cycle is

given by

$$\sigma_{hyst}^{t,c} = \pm \frac{3}{2} \left(\frac{d_c^+ + d_c^-}{g_i^{\frac{1}{3}}} \right) \left(\left(\frac{2}{3} \right)^{\frac{5}{2}} \pm \frac{2}{27} b_i \right)^{\frac{1}{3}}, \quad (5.8)$$

with the choice of positive sign for tension and negative for compression.

We now make a series of comments about these results and the various parameters of the model. We first consider the critical stress for transformation $\sigma_{MS}^{t,c}$ given in (5.4). This stress depends on temperature through the function $\omega(\theta)$. If this is linear as is commonly assumed with the slope related to the latent heat, then the critical stress for transformation will also change linearly with the temperature with the slope related to the latent heat. This is consistent with various experimental observations [48]. We also see that at any given temperature, the parameter g_i controls the value of this critical stress for transformation in both tension and compression, while the parameter b_i independently controls the difference in the value between tension and compression. Thus, parameter b_i is responsible for the asymmetry in stress between tension and compression. We now turn to the transformation strain described in (5.6). Note that this depends on the parameters g_s and b_s , and is thus completely independent of the critical stress for transformation. The parameter g_s controls the magnitude of this strain in both tension and compression while the parameter b_s controls the difference between tension and compression. Finally, the parameters d_c^\pm control the amount of stress hysteresis, see (5.8). In summary, the model has enough freedom to assign the critical stress, the transformation strain, and stress hysteresis independently, and independently in tension and compression.

5.2 Simple Shear

We now turn to simple shear, and show that the parameters b_i and b_s have a more subtle effect on the transformation strains and cause the transformation strain to be nonparallel to the applied stress even in the isotropic setting. As before we work at a constant temperature well above the transformation temperature and start with $\lambda = 0$. We apply an increasing stress of the form

$$\sigma = \begin{pmatrix} 0 & 0 & 0 \\ 0 & 0 & \tau \\ 0 & \tau & 0 \end{pmatrix}.$$

As the stress increases, the nominal transformation strain increases to its optimal value with the set of constraints. By symmetry, it has the general form

$$\varepsilon_m = \begin{pmatrix} -x - z & 0 & 0 \\ 0 & z & y \\ 0 & y & x \end{pmatrix}.$$

To find the specific value, we need to find the point where the normal to $\partial\mathcal{G}_i$ is parallel to the applied stress, or $\partial G_i/\partial\varepsilon_m$ is parallel to σ . One has to be careful in this differentiation since it has to be carried out and interpreted in the space of trace-free matrices. Thus, if one differentiates these functions in the space of matrices, one has to project the derivative on to the space of trace-free matrices, or

$$\mathbb{P}\left(\frac{\partial G_i}{\partial\varepsilon_m}\right) \parallel \sigma,$$

where \mathbb{P} is the projection to the space of trace-free matrices. In our case, the derivative of the determinant in the space of matrices gives the cofactor, and the cofactor of trace-free matrices need not be trace-free. Working through these details, we find that this condition is satisfied if and only if the parameters x, y, z satisfy:

$$\begin{aligned} 2Ez - \frac{2}{3}zx - \frac{2}{3}x^2 + \frac{1}{3}y^2 + \frac{1}{3}z^2 &= 0, \\ 2Ex - \frac{2}{3}zx + \frac{1}{3}x^2 + \frac{1}{3}y^2 - \frac{2}{3}z^2 &= 0. \end{aligned} \tag{5.9}$$

where $E = |\varepsilon_m| b_i$. Subtracting the second equation above from the first yields the condition

$$2E(z - x) - x^2 + z^2 = 0 \iff -2E(x - z) = (x + z)(x - z).$$

This leaves two possibilities, $(x - z) = 0$ and $(x + z) = -2E$. The latter possibility implies that $\partial G_i / \partial \varepsilon_m$ is identically zero and is hence rejected. We conclude that $x = z$

$$\varepsilon_m = \begin{pmatrix} -2x & 0 & 0 \\ 0 & x & y \\ 0 & y & x \end{pmatrix},$$

Substituting it back into (5.9) and doing some manipulation yields

$$\left(\frac{24}{b_i^2} - 1\right)x^4 + \left(\frac{8}{b_i^2} + \frac{2}{3}\right)x^2y^2 - \frac{1}{9}y^4 = 0.$$

We have to solve this simultaneously with the condition that $\varepsilon_m \in \partial \mathcal{G}_i$ or

$$\frac{2}{3}(6x^2 + 2y^2)^{\frac{3}{2}} + b_i(2xy^2 - 2x^3) - g_i = 0,$$

for x, y .

Unfortunately, we are unable to solve this in closed form. Yet, the above equations reveal two important features. First, except in the case $b_i = 0$, applied simple shear gives rise to nontrivial normal components in the nominal transformation strain even in the isotropic situation. This is akin to the Poynting effect, and implies that the normal boundary constraint is critical in studying torsion. Second, notice that these conditions are impervious to the change of sign of σ . This is true in all aspects, and thus there is no asymmetry with respect to sign unlike in uniaxial extension.

Once we know the optimal nominal transformation strain ε_m^0 , we can use it to determine driving force and in turn the stress at which the onset of transformation begins. As the transformation proceeds and λ increases until the effective transformation strain $\lambda\varepsilon_m^0$ saturates the constraint \mathcal{G}_s . However, depending on the values b_i and b_s , $\lambda\varepsilon_m^0$ may not be the matrix that is optimal in \mathcal{G}_s for the applied load. If it is not, the martensite reorients and begins the nominal transformation strain ε_m changes until $\lambda\varepsilon_m$ is optimal in \mathcal{G}_s for the applied load. Thus, a misorientation of \mathcal{G}_i and \mathcal{G}_s can lead to realignment of martensite.

5.3 Combined Uniaxial Extension and Shear

We now turn to strain-controlled experiments combining uniaxial extension and shear. This loading protocol is motivated by the combined tension-torsion of a tube. As before we consider an isotropic situation well above the transformation temperature and begin with a specimen completely in the austenite. We load it until transformation begins and saturates, and then unload it completely.

The algebra becomes too difficult, and we therefore resort to numerical studies. Since hard constraints are difficult to implement numerically, we replace the hard

constraints, (3.10), (3.11) with the following high order polynomials:

$$G_{i,s}(\xi) = \left(\frac{\frac{2}{3}(\xi \cdot \xi)^{3/2} + b_{i,s} \det(\xi) + \frac{1}{3}c_{i,s} |e_{i,s}^{\hat{\cdot}} \cdot \xi e_{i,s}^{\hat{\cdot}}|^3}{g_{i,s}} \right)^{16}. \quad (5.10)$$

We shall have a opportunity to evaluate the influence of this constraint presently

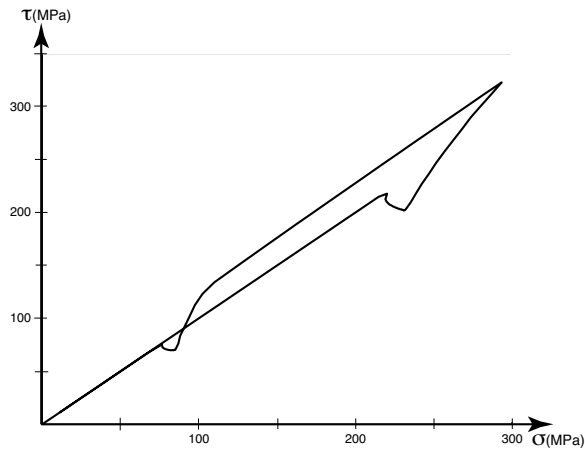
We begin in the isotropic situation ($c_i = c_s = 0$) with a strain-control test where we apply a strain of the form

$$\varepsilon = \begin{pmatrix} 0 & 0 & 0 \\ 0 & 0 & \gamma(t) \\ 0 & \gamma(t) & \varepsilon(t) \end{pmatrix}, \quad (5.11)$$

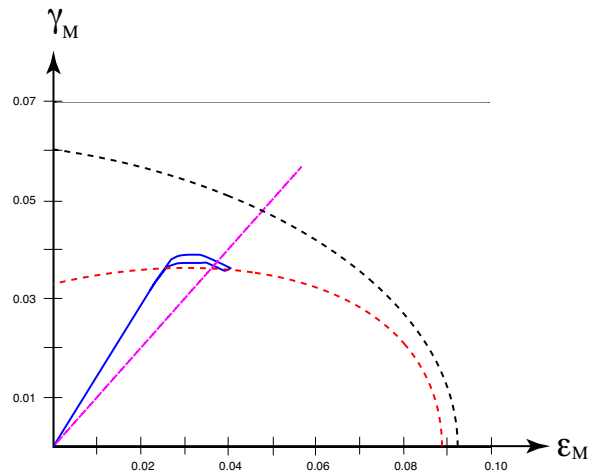
with $\gamma(t) = c\varepsilon(t)$. In this case c is chosen to be equal to 1.

Figure 5.1(a) shows the resulting trajectory of the stress where σ denotes the uniaxial (33) component and τ the shear (23) component. Note that the stress components (σ - τ) are not proportional although the applied strain components (ε - γ) are. This is consistent with the experimental observations of Anand and Thamburaja and Jung [64], [43].

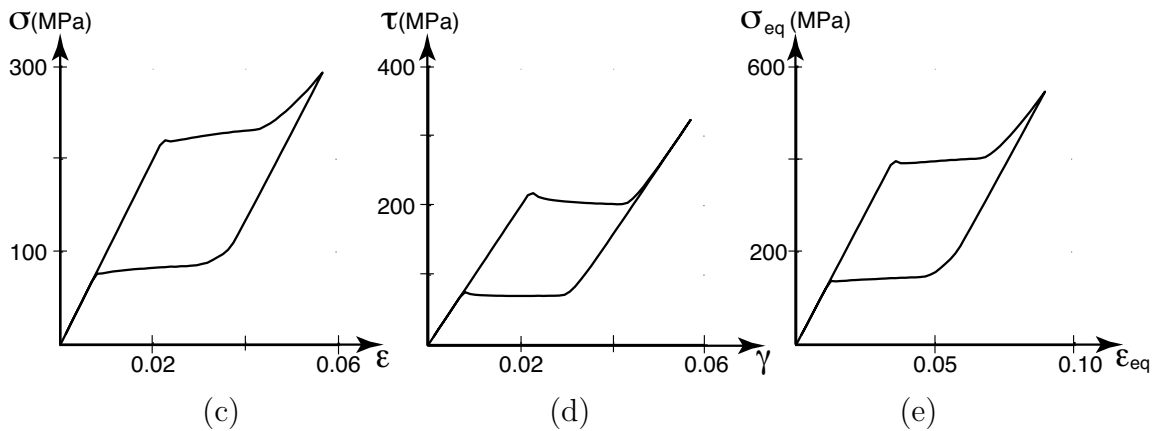
The underlying reason for this non-proportionality is the reorientation of martensite, and this is clear in the space of transformation strains shown in figure 5.1(b). This figure shows the trajectory of the normal and shear components of the effective transformation strain in blue bold line, the constraint \mathcal{G}_t on the nominal transformation strain as the dashed black arc and the constraint \mathcal{G}_s on the effective transformation strain as the dotted red arc. It also shows the imposed strain direction as the purple dashed line. The effective transformation strain starts out at zero and gradually increases in a direction that is optimal for the applied load. Thus the original



(a)



(b)



(c)

(d)

(e)

Figure 5.1: A proportional strain-controlled extension-shear test of an isotropic material. (a) The resulting stress, (b) the resulting transformation strain along with a verification of the numerical method, (c) uniaxial stress vs. uniaxial strain (d) shear stress vs. shear strain and (e) equivalent stress vs. equivalent strain.

direction depends on the nominal transformation strain and thus on the shape of the set \mathcal{G}_i . Therefore it can be-and is so in this case-different from the direction of the applied total strain. The effective transformation strain increases along this direction as the transformation proceeds until it encounters the boundary of the set \mathcal{G}_s . It then tries to optimize itself within this latter set and this results in reorientation of the martensite, and this is clearly visible in this case. It also causes the observed reorientation in the direction of stress.

Note that we have reorientation of martensite in this case even though it is isotropic. The determinant-dependant terms (those with the coefficients $b_{i,s}$) that were responsible for the tension-compression asymmetry enable the initiation and the saturation surfaces to be eccentric.

Figure 5.1(c-e) show the stress-strain curve in components and in equivalent form. Note that these curves can look quite different in the normal and the shear directions. In particular, the shear curve appears to have a negative slope. This is because the reorientation of martensite gives rise to a significant change in the shear component of the transformation strain. However, the negative slope does not necessarily signal an instability.

We conclude with a comment on the softened polynomial constraint (5.10). Figure 5.1(b) plots the surfaces according to the hard constraint, and we see that the trajectory computed with the soft constraint tracks is quite closely. We also see a little overshoot in the stress-strain curves due to the numerical method.

5.4 Anisotropic Materials

The discussion has until now focused on isotropic materials. We now consider uniaxial or transversely isotropic materials subjected to combined extension along the

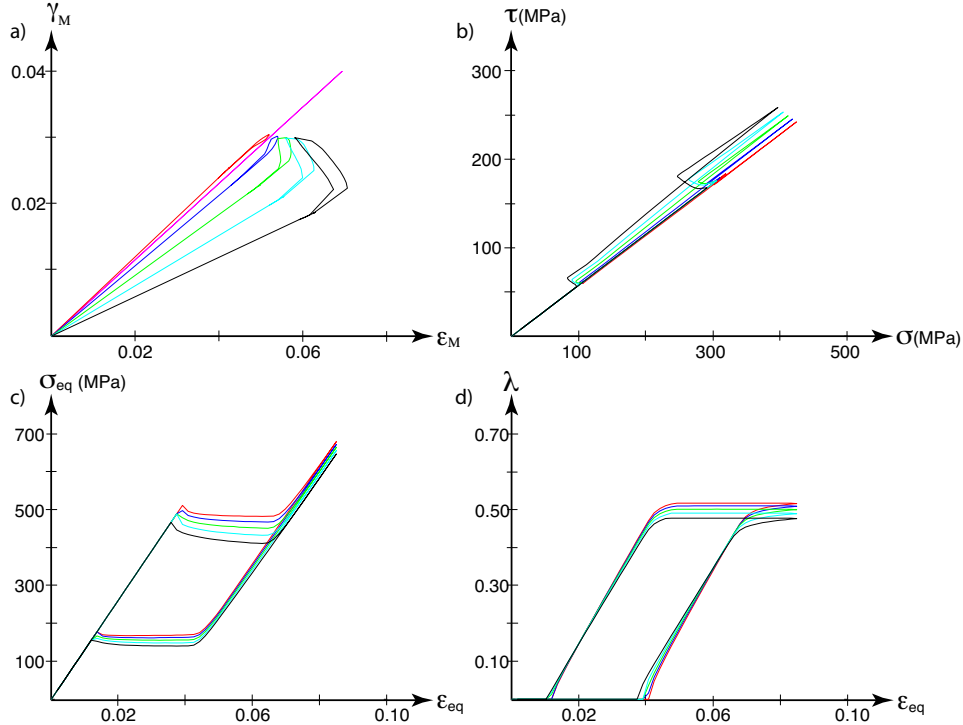


Figure 5.2: Anisotropy of the initiation surface. Combined extension and shear of an uniaxial material under strain control for various values of c_i ranging from 0.3-1.5. (a) The effective transformation strain trajectory. The applied strain trajectory is indicated by the dashed line. (b) The stress trajectory, (c) equivalent stress vs. equivalent strain (d) volume fraction vs. equivalent strain.

axis of symmetry and shear. In other words, we set $e_i = e_s = e_3$ with c_i, c_s possibly non-zero and apply a strain of the form (5.11).

Figure 5.2 shows the results for increasing anisotropy of the initiation surface or various values of c_i ranging from 0.3 to 1.5 (by equally spaced increments) for $c_s = b_i = b_s = 0$. When $c_i = 0$, the initiation and saturation surfaces are coaxial and aligned. Thus there is no reorientation of martensite and the transformation strain and stress are proportional and is close to the direction of applied strain (the small difference depends on the elastic modulus). When c_i is non-zero, the initiation

surface is eccentric. Therefore the optimal nominal transformation strain deviates in direction from that of the applied strain. Thus, the effective strain trajectory starts out on a different direction, though the stress appears to maintain the same direction. Further, the initiation and saturation surfaces are no longer aligned. Thus, when the effective transformation strain is large enough, we see reorientation of the martensite, and consequently non-proportional transformation strain and stress. Further, for high values of c_i , we see that the equivalent stress-equivalent strain curve shows a downward slope. However, this does not indicate any instability. Finally, we see that the transformation is not complete even for large stresses.

Figure 5.3 shows the results of anisotropy in the saturation surface various values of c_s ranging from 0.3 to 1.5 in equal increments for $c_i = b_i = b_s = 0$. Since the initiation surface is held fixed, each trajectory of the effective transformation strain starts out in the same direction. However, the saturation and reorientation depends on the value of c_s . The amount of reorientation happens to be less dramatic than in the previous situation.

Figure 5.4 shows the results of anisotropy in both the initiation and saturation surfaces. It proportionally varies the parameters c_i, c_s in the range 0.3 to 1.5. The trajectory of the effective transformation strain shows features of the earlier cases, the directions start out differently and the reorientation is quite significant.

5.5 Proportional Loading in Different Directions

In the previous set of simulations, we saw that the geometry of initiation and saturation surfaces have a significant effect on the overall hysteretic behavior of the material as well as the reorientation of martensitic transformation strain. We now examine the role of loading direction. We fix the initiation surface by fitting it to the

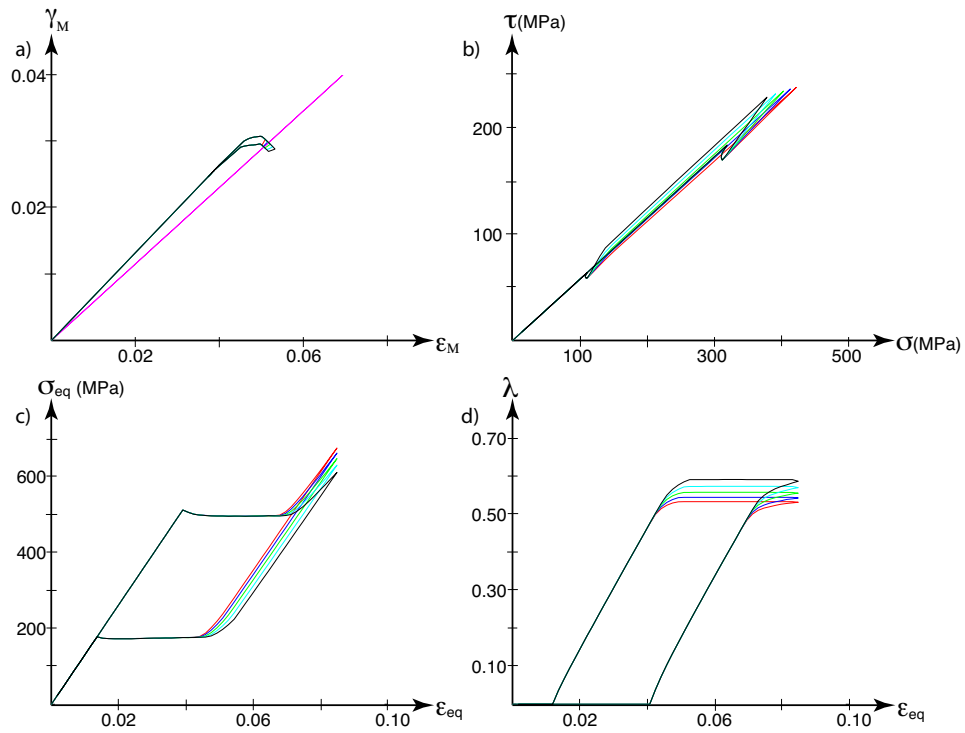


Figure 5.3: Anisotropy of the saturation surface. Combined extension and shear of an uniaxial material under strain control for various values of c_s ranging from 0.3 to 1.5. (a) The effective transformation strain trajectory. The applied strain trajectory is indicated by the dashed line. (b) The stress trajectory, (c) equivalent stress vs. equivalent strain, (d) volume fraction vs. equivalent strain.

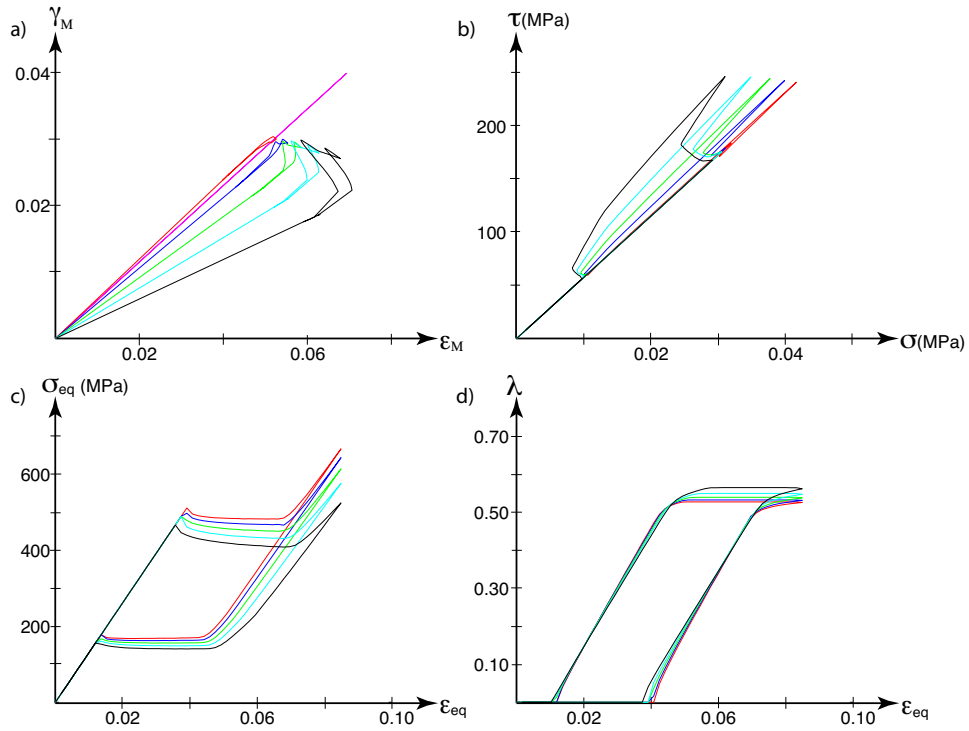


Figure 5.4: Anisotropy of the both surfaces. Combined extension and shear of an uniaxial material under strain control for various values of c_i, c_s ranging from 0.3 to 1.5 (in equal increments). (a) The effective transformation strain trajectory. The applied strain trajectory is indicated by the dashed line. (b) The stress trajectory, (c) equivalent stress vs. equivalent strain, (d) volume fraction vs. equivalent strain.

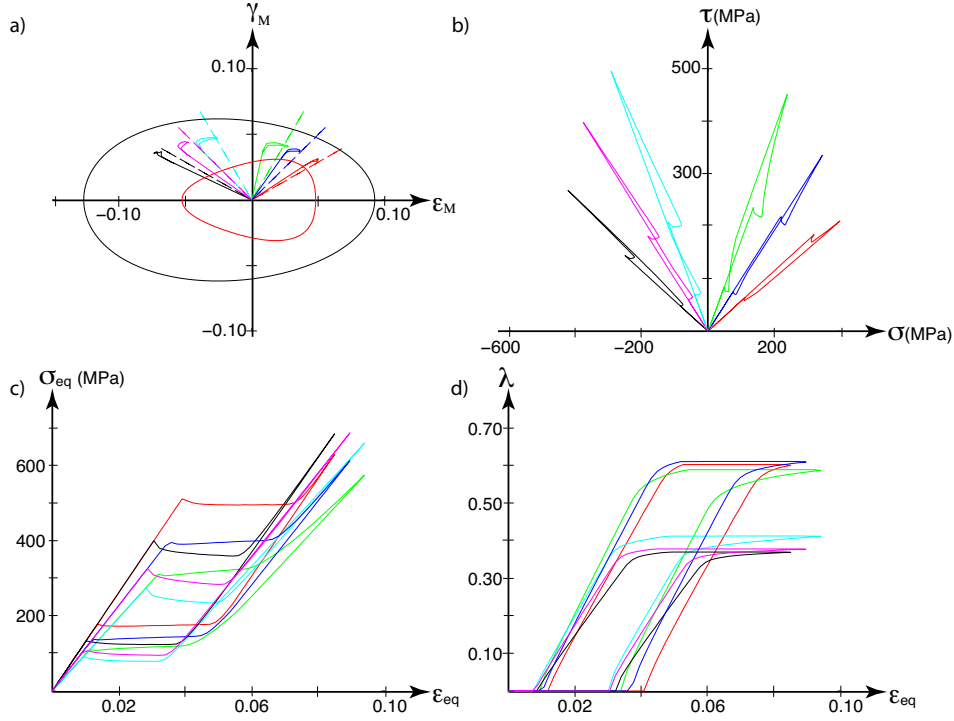


Figure 5.5: Variation of direction applied strain. (a) The effective transformation strain trajectory. The applied strain trajectories are indicated by the dashed lines. (b) The stress trajectory, (c) equivalent stress vs. equivalent strain, (d) volume fraction vs. equivalent strain.

experimental results of Lexcellent and the saturation surface. Specifically, $b_i = -1.8$, $g_s = 2.05 \times 10^{-4}$. A slight eccentricity (coaxial) and asymmetry have been added to the saturation surface to underscore the effect of these parameters on the martensitic reorientation: $b_s = 1.0$, $c_s = 1.5$, and $g_s = 2.25 \times 10^{-5}$.

Figure 5.5 shows the response of the material for proportional applied strain with different ratios of extension and shear. The direction of applied strain in the various cases are indicated by the dashed lines, and the resulting trajectory of the effective transformation strain is shown in the continuous line of the same color in figure 5.5(a). The two surfaces as well as the trajectory of the effective transformation

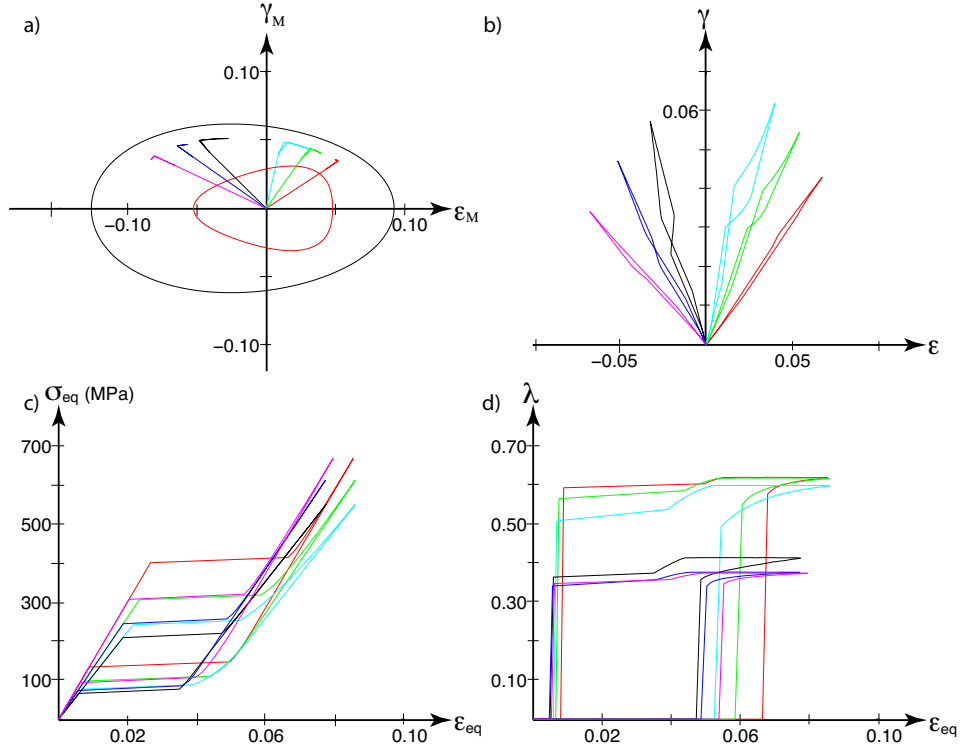


Figure 5.6: Variation of direction applied stress. (a) The effective transformation strain trajectory. (b) The stress trajectory, (c) equivalent stress vs. equivalent strain, (d) volume fraction vs. equivalent strain.

strain are also shown. We see that the amount of deviation between the direction of the applied strain and the initial direction of the transformation strain (which arises due to the large distortion of the initiation surface normal vectors due to the considerable determinant term added to incorporate the tension-compression asymmetry) as well as the amount of reorientation of martensite varies considerably with loading direction. The resulting equivalent strain-equivalent stress curves also vary significantly. Importantly, the amount of transformation or the volume fraction of martensite on saturation depends significantly on the loading direction. This will turn out to be very important when we consider nonproportional tests.

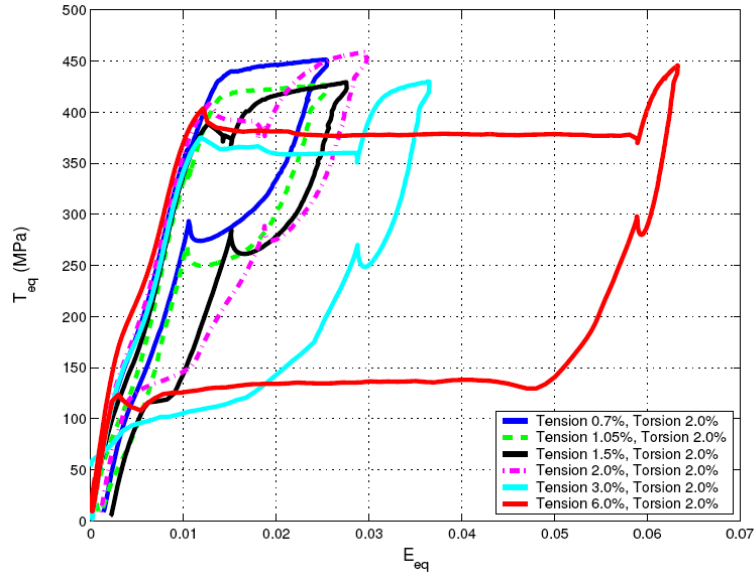


Figure 5.7: The experimental observations of Jung [36] show the emergence of secondary hysteresis in nonproportional tension-torsion.

Figure 5.6 shows the corresponding response in stress control. The observed features are similar.

5.6 Nonproportional Loading

The fact that the response of the material can be different in different directions motivates us to study nonproportional loads. An interesting case are the experimental observations of Jung [36] reproduced in figure 5.7. They were studying the combined tension and torsion of thin walled tubes, and observed a dual plateau for when they applied a uniaxial extension followed by torsion. Thin-walled NiTi tubes (0.37 mm wall thickness) were loaded slowly ($10^{-5}s^{-1}$ to $10^{-4}s^{-1}$) avoid rate effects. The loading program followed was to load to tensile strain of 6% followed by a torsional strain

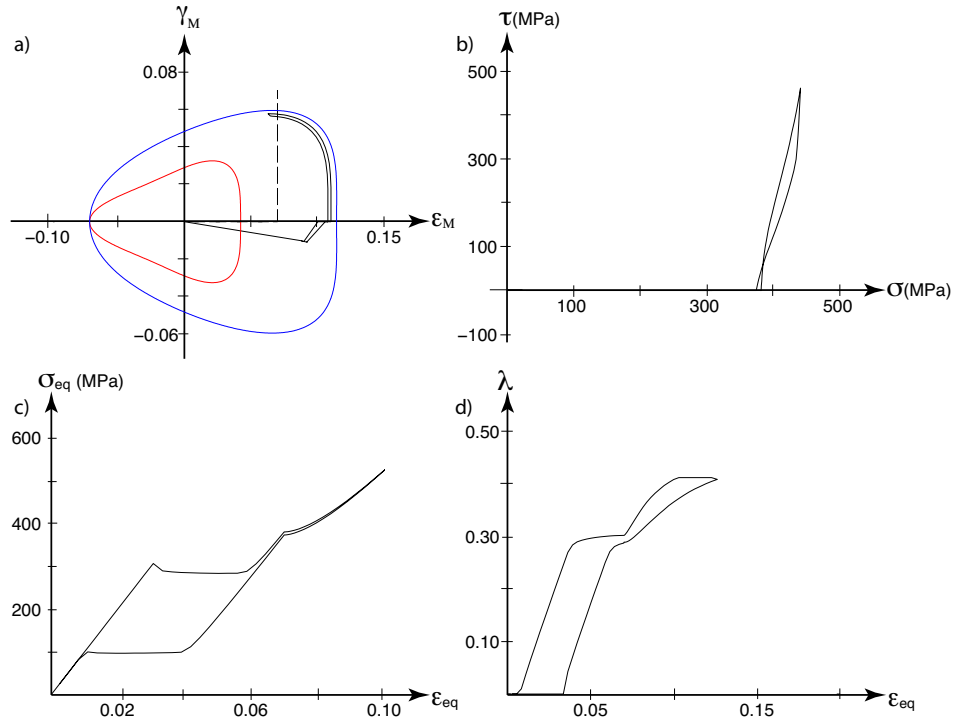


Figure 5.8: Dual plateau in nonproportional loading. (a) The effective transformation strain trajectory. The applied strain trajectories are indicated by the dashed lines. (b) The stress trajectory, (c) equivalent stress vs. equivalent strain, (d) volume fraction vs. equivalent strain.

of 2%. The unloading was in the reverse order (torsion unloads before tension). Unfortunately, they do not provide enough details for us to fit our model completely. Thus, we are left to examine the situation qualitatively. Figure 5.8 shows the results of a simulation that reproduces this dual plateau. The initiation and saturation surfaces are chosen to display marked asymmetry. As the applied strain increases in the normal direction, the transformation begins and saturates. Thus the stress shows a plateau and then begins to increase. Now, we apply shear. The martensite begins to reorient with the stress at a more or less constant volume fraction until it reaches a highly curved section. Sufficient reorientation now makes it possible to have additional transformation, and thus gives rise to the second plateau.

This reasoning also indicated why, when the thin tubes were loaded in torsion first and then tension, dual plateaus were not observed. In the shear direction, the transformation saturates at a higher value of λ . When the tensile strain is applied, the headroom in the phase fraction that was available in the previous loading program is not available. No more stress relief can take place due to transformation. A secondary plateau is unable to emerge.

We conclude the parameter study by displaying the results of a circular and square loading path in figures 5.9 and 5.10 respectively. In these results, the initiation and saturation surfaces are set to be those in the previous subsection.

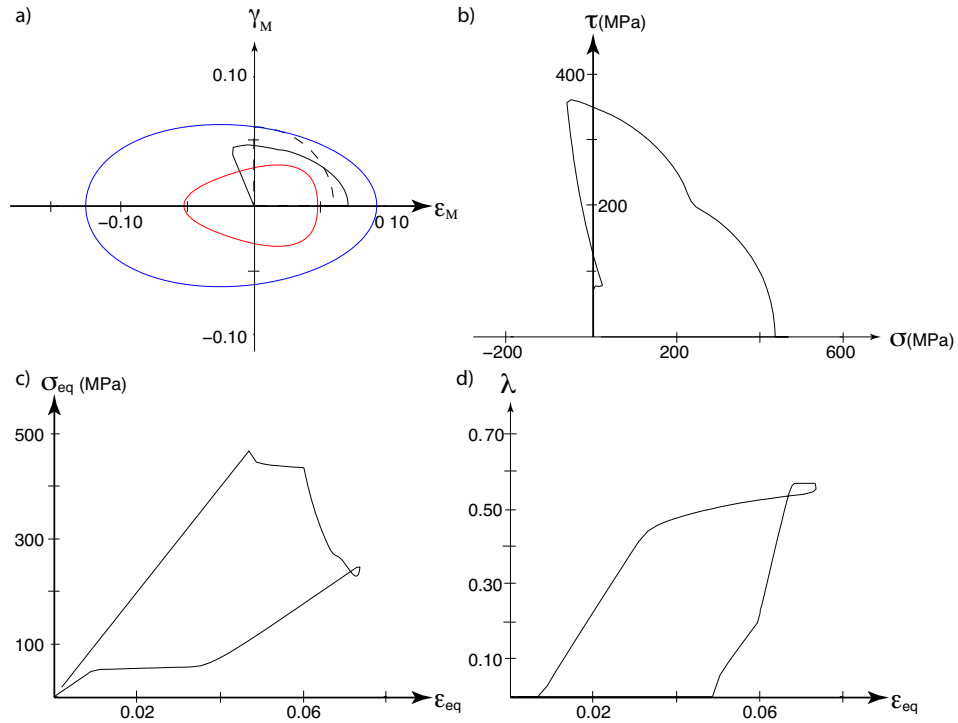


Figure 5.9: Circular Loading Path. (a) The effective transformation strain trajectory. The applied strain trajectories are indicated by the dashed lines. (b) The stress trajectory, (c) equivalent stress vs. equivalent strain, (d) volume fraction vs. equivalent strain.

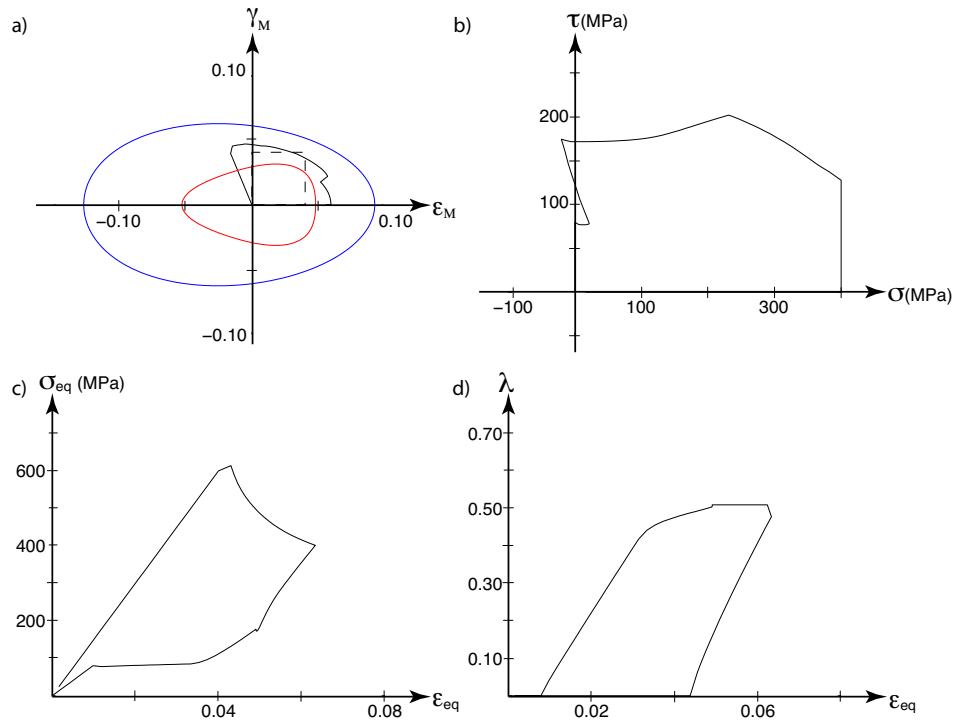


Figure 5.10: Square Loading Path. (a) The effective transformation strain trajectory. The applied strain trajectories are indicated by the dashed lines. (b) The stress trajectory, (c) equivalent stress vs. equivalent strain, (d) volume fraction vs. equivalent strain.

Chapter 6

Numerical Implementation and Example

In the bigger picture, in order for the model to be of use in an engineering context, it should be implementable in a finite-element package. To utilize the model on the scale of engineering applications, an UMAT for the ABAQUS package was developed. Given the strain control field ϵ^t , the fields ϵ_M^t and λ^t are found by the implicit minimization scheme at each time step and node:

$$\lambda^{t+1}, \epsilon_M^{t+1} = \arg \min_{\epsilon_M^{t+1} \in \mathcal{G}_i, \lambda^{t+1} \epsilon_M^{t+1} \in \mathcal{G}_s} \left\{ \frac{1}{2} (\epsilon^{t+1} - \lambda^{t+1} \epsilon_M^{t+1}) : \mathbf{C} (\epsilon^{t+1} - \lambda^{t+1} \epsilon_M^{t+1}) + \lambda^{t+1} \omega(\theta) + G_i (\epsilon_M^{t+1}) + G_s (\lambda^{t+1} \epsilon_M^{t+1}) + \Delta t \varphi^* \left(\frac{\lambda^{t+1} - \lambda^t}{\Delta t} \right) \right\}. \quad (6.1)$$

Here the function $\varphi^*(\dot{\lambda})$ is the Legendre transform of the dissipation potential associated with each kinetic law (i.e., $\dot{\lambda} = \frac{\partial \varphi(d\lambda)}{\partial d\lambda}$). Examples of these potentials can be written in the stick-slip case and the rate-independent one.

i) Stick-slip (the case $p = 2$)

$$\varphi^*(\dot{\lambda}) = \begin{cases} \dot{\lambda} d_c^+ + \frac{\dot{\lambda}^3 \lambda_+}{\lambda_+^2 - \dot{\lambda}^2} + \frac{\dot{\lambda}_+}{2} \ln \left(\frac{\dot{\lambda}^2}{\lambda_+^2 - \dot{\lambda}^2} + \frac{1}{2} + \sqrt{\left(\frac{\dot{\lambda}^2}{\lambda_+^2 - \dot{\lambda}^2} \right)^2 + \left(\frac{\dot{\lambda}^2}{\lambda_+^2 - \dot{\lambda}^2} \right)} \right) \\ \quad - \dot{\lambda}_+ \sqrt{\left(\frac{\dot{\lambda}^2}{\lambda_+^2 - \dot{\lambda}^2} \right)^2 + \left(\frac{\dot{\lambda}^2}{\lambda_+^2 - \dot{\lambda}^2} \right)} & \dot{\lambda} \geq 0 \\ -\dot{\lambda} d_c^- + \frac{-\dot{\lambda}^3 \lambda_-}{\lambda_-^2 - \dot{\lambda}^2} + \frac{-\dot{\lambda}_-}{2} \ln \left(\frac{\dot{\lambda}^2}{\lambda_-^2 - \dot{\lambda}^2} + \frac{1}{2} + \sqrt{\left(\frac{\dot{\lambda}^2}{\lambda_-^2 - \dot{\lambda}^2} \right)^2 + \left(\frac{\dot{\lambda}^2}{\lambda_-^2 - \dot{\lambda}^2} \right)} \right) \\ \quad + \dot{\lambda}_- \sqrt{\left(\frac{\dot{\lambda}^2}{\lambda_-^2 - \dot{\lambda}^2} \right)^2 + \left(\frac{\dot{\lambda}^2}{\lambda_-^2 - \dot{\lambda}^2} \right)} & \dot{\lambda} \leq 0 \end{cases} \quad (6.2)$$

ii) Rate-independent kinetics

$$\varphi^*(\dot{\lambda}) = \begin{cases} d_c^+ \dot{\lambda} & \dot{\lambda} \geq 0 \\ d_c^- \dot{\lambda} & \dot{\lambda} \leq 0 \end{cases} \quad (6.3)$$

These potentials can be seen in figure 6.1. Here, for the sake of convenience, the simplifying assumption that $d_c^- = -d_c^+$ has been made.

In order to make the constraints differentiable, they are implemented using standard penalties:

$$G_i = \left(\frac{\frac{2}{3}(\varepsilon_M \cdot \varepsilon_M)^{3/2} + b_i \det(\varepsilon_M) + \frac{1}{3}c_i |\hat{e}_i \cdot \varepsilon_M \hat{e}_i|^3}{g_i} \right)^N, \quad (6.4)$$

$$G_s = \left(\frac{\frac{2}{3}(\lambda \varepsilon_M \cdot \lambda \varepsilon_M)^{3/2} + b_s \det(\lambda \varepsilon_M) + \frac{1}{3}c_s |\hat{e}_s \cdot \lambda \varepsilon_M \hat{e}_s|^3}{g_s} \right)^N, \quad (6.5)$$

where N is some large, positive, even exponent; in this case taken to be 16.

The effect of this smoothing constraint is to generally overestimate the set of admissible transformation strains. As is seen in the figure 6.2, the intersection of the polynomial constraint and the quadratic elastic energy is shifted slightly outward

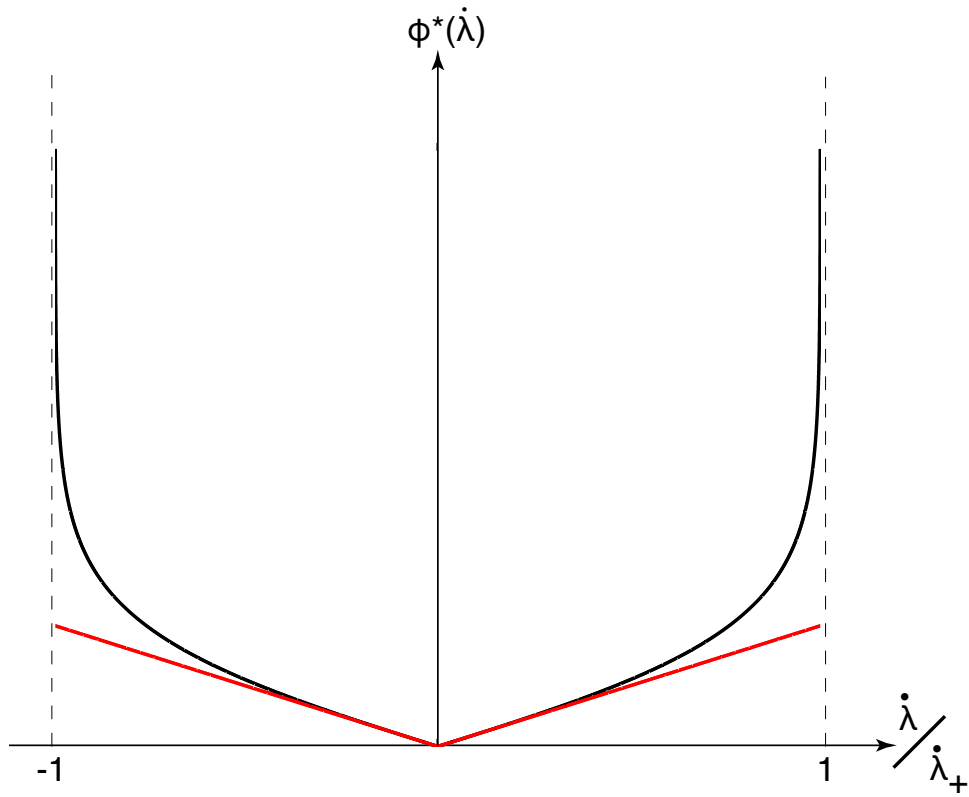


Figure 6.1: The Legendre transform of the dissipation potentials are shown in the stick-slip case (black) for $p = 2$ and in the rate-independent case (red).

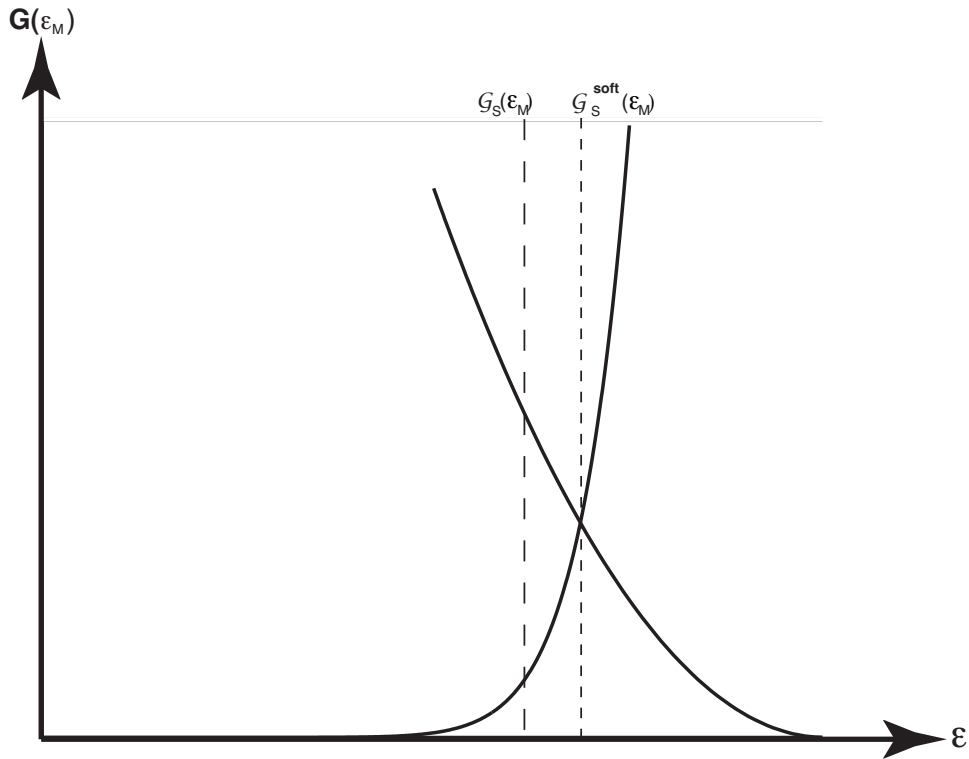


Figure 6.2: The effect of the polynomial constraint is seen. The intersection of the 16th degree polynomial shifts the intersection point with the quadratic elastic energy slightly to the right of the hard (dashed) constraint.

from the hard constraint (dashed well). Naturally, increasing the degree N of the constraining polynomial will make the value of strain at which this intersection occurs closer to that of the hard constraint. The trade-off is that the derivative of the constraint polynomial becomes increasingly steep with N , making it harder to deal with in a conjugate gradient scheme.

The result of this softening can be seen in terms of the total transformation strain in the polycrystal in figure 6.3. The dashed green set represents the ideal saturation constraint G_s . The red dashed curve is the scaled constraint set at λ_{sat} . The solid red set represents the softened ($N = 16$) constraint for 10% strain applied in each

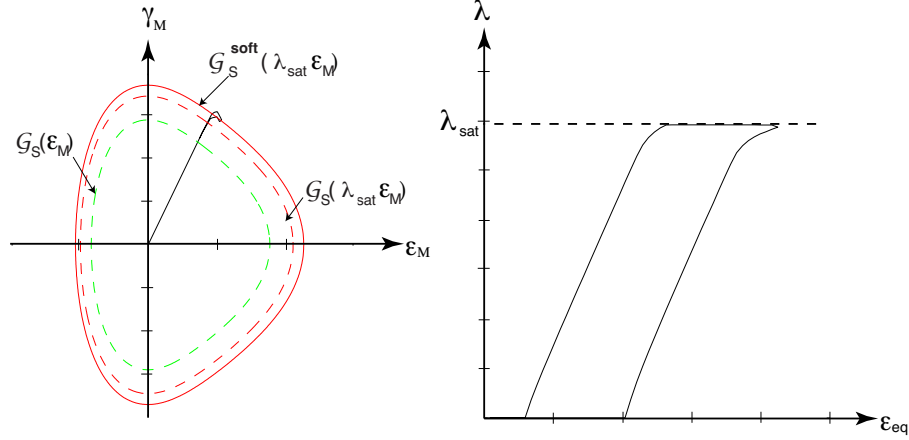


Figure 6.3: The smoothed constraint set is calculated at 10% applied strain. The green dashed constraint is \mathcal{G}_s , the red dashed constraint is the scaled \mathcal{G}_s at $\lambda = \lambda_{sat}$ and the red solid set is the softened polynomial ($N = 16$) constraint at λ_{sat} .

direction in the tension-shear plane. Even at large values of applied strain, the error introduced by softening the constraint does not seem very significant.

With each component in the energy smoothed, the implicit minimization of the nodal energy is conducted using a nested conjugate gradient scheme in the (λ, ε_M) space. With the transformation strain and volume fraction fields attained through minimization, the nodal stress values ($\sigma = \mathbf{C} : (\varepsilon - \lambda \varepsilon_M)$) are computed trivially. The linearized strain assumption also allows for simple computation of the tangent modulus ($\frac{\partial \sigma}{\partial \varepsilon}$). It should be noted that the contribution of the initiation and saturation surfaces is incorporated into the tangent modulus through the $\frac{\partial \varepsilon}{\partial \varepsilon_M}$ term, the value of which is calculated by exploiting the fact that the energy density is at a stationary point ($\delta W = 0$) and implicitly differentiating.

Because one of the current areas of interest in the application of shape memory alloys for engineering is in the biomedical field, this area was selected as a sufficiently fashionable one for a demonstration of the finite-element implementation of

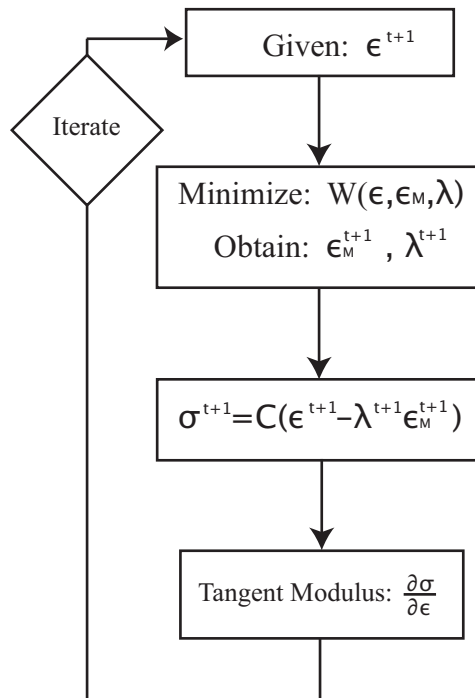


Figure 6.4: A flowchart of the numerical implementation

the model. A beam element of a NiTiNOL stent was examined in an ABAQUS simulation in pure bending with symmetry boundary conditions as shown below.

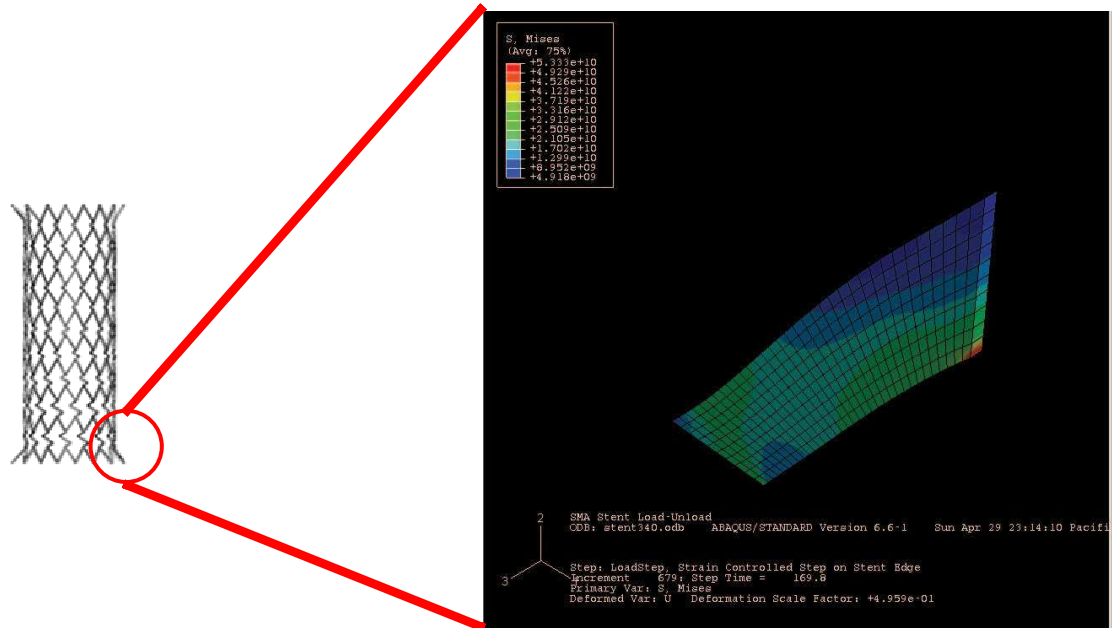


Figure 6.5: An example of the finite-element implementation on a stent element.

Chapter 7

Conclusions and Future Directions

Shape-memory alloys demonstrate interesting nonlinear thermoelastic behaviors including superelasticity and the shape-memory effect. These behaviors find their origin in the formation of microstructure. We have proposed a constitutive model of these materials in which the strain associated with microstructural formation (ε_M) is constrained to lie within two interacting sets. The two constraint sets arise from the fundamental difference in mechanics between the initiation of martensitic transformation and its saturation: the initiation constraint being a Sachs (or Reuss) type constant stress bound on the set of admissible transformation strains, and the saturation constraint a Taylor (or Voigt) constant strain bound. The interaction of these two constraints in the model have been shown to result in several well-known features of SMAs including superelasticity, shape-memory, reorientation of martensite, and retention of austenite.

The geometry of the constraint sets has a great effect on the response of the SMA polycrystal. This was examined in detail in parameter studies in proportional and nonproportional loading, in stress and strain controlled simulations. Varying the constraint shapes had a large effect on the tension-compression asymmetry, reorientation of the martensite, and the amount of retained austenite. In nonproportional

loading, the geometry of the constraints could be manipulated to give rise to the curious secondary stress plateau observed experimentally. The parameter studies indicate that, as an alternative to deriving the Sachs and Taylor bounds of the polycrystal, they can be recovered by fitting an appropriate set of functions to known experiments.

The development of the model with only one constrained deviatoric tensorial variable (ε_M) for recoverable strain, and one scalar (λ) for martensitic phase fraction, results in a low-dimensional numerical implementation which can be easily incorporated into commercial finite-element packages (in this case ABAQUS). The development of a UMAT for the proposed model serves as a proof of the concept in a currently relevant design software.

Although this constitutive model reproduces many experimental characteristics of SMAs in a compact and robust way, it is unable to reproduce the well-known phenomena of localization or the formation of martensite transformation bands. Initially it was hoped that banding phenomena could be reproduced in sets of sufficiently different eccentricity; rapid reorientation giving rise to macroscopic instability. This no longer seems to be a fruitful direction for inquiry as all numerical investigations have failed to yet yield such an instability. Instead a possible future pursuit would be to attempt to explain banding as a mesoscale process; for instance as a grain-scale percolation phenomenon.

Another limitation of the current model is that it is not easily extended to the regime of finite deformation. The general notion of interacting constraint sets can be incorporated in a finite deformation framework. The meaning of the Sachs and Taylor bounds are no longer as clear cut however. The constant strain bound especially no longer serves as a good approximation of the total recoverable strain of the polycrystal. The further complication that the strains are no longer additive

($\varepsilon = \varepsilon_{elast} + \lambda\varepsilon_M$), but multiplicative in their composition ($\mathbf{F} = \mathbf{F}_e\mathbf{F}_M$) means that the effect of λ on the transformation strain can no longer be assumed to be linear. Future investigation of these bounds on the nonlinear polycrystal is an obvious avenue of future interest. In addition a more ad hoc extension of the model to finite deformations might be useful for design purposes in regimes where experimental data exists.

Bibliography

- [1] ABAQUS. Umat and vumat routines for the simulation of nitinol. *Answer ID 1658*, ABAQUS Inc. , Pawtucket, RI.
- [2] R. Abeyaratne, C. Chu, and R. D. James. Kinetics of materials with wiggly energies: Theory and application to the evolution of twinning microstructure in a cu-al-ni alloy. *Phil. Mag. A*, 73:457–497, 1996.
- [3] R. Abeyaratne and J. K. Knowles. On the driving traction on a surface of a strain discontinuity in a continuum. *J. Mech. Phys. Sol.*, 38:345–360, 1990.
- [4] R. Abeyaratne and J. K. Knowles. A continuum model of a thermoelastic solid capable of undergoing phase-transitions. *J. Mech. Phys. Sol.*, 41:541–571, 1993.
- [5] F. Auricchio and R. I. Taylor. Shape-memory alloys: modelling and numerical simulations of the finite-strain superelastic behavior. *Comp. Methods Appl. Mech. Eng.*, 143:175–194, 1997.
- [6] J. Ball. Convexity conditions and existence theorems in nonlinear elasticity. *Arch. Rat. Mech. Anal.*, 63:337–403, 1977.
- [7] J. Ball, C. Chu, and R. D. James. Hysteresis during stress-induced variant rearrangement. *J. Phys. IV France*, 5:245–251, 1995.

- [8] J. Ball and R. D. James. Fine phase mixtures as minimizers of energy. *Arch. Rat. Mech. Anal.*, 100:13–52, 1987.
- [9] J. Ball and R. D. James. Proposed experimental tests of a theory of fine microstructure and the two-well problem. *Phil. Trans. R. Soc. Lond. A*, 338:389–450, 1992.
- [10] K. Bhattacharya. Comparison of the geometrically nonlinear and linear theories of martensitic transformation. *Cont. Mech. and Therm.*, 5:205–242, 1993.
- [11] K. Bhattacharya. Phase boundary propagation in heterogeneous bodies. *Proc. Roy. Soc. Lond. A*, 455:757–766, 1999.
- [12] K. Bhattacharya. *Microstructure of Martensite: Why it Forms and How it Gives Rise to the Shape-Memory Effect*. Oxford University Press, 2004.
- [13] K. Bhattacharya and R.V. Kohn. Energy minimization and the recoverable strains of polycrystalline shape-memory alloys. *Arch. Rational Mech. Anal.*, 139:99–180, 1997.
- [14] K. Bhattacharya, P. Purohit, and B. Craciun. The mobility of twin and phase boundaries. *J. Phys. IV France*, 112:163–166, 2003.
- [15] K. Bhattacharya and A. Schlömerkemper. Transformation yield surface of shape memory alloys. *J. Phys. IV France*, 115:155–162, 2004.
- [16] K. Bhattacharya and A. Schlömerkemper. Stress-induced phase transformations in shape-memory polycrystals. *In preparation*, 2008.

- [17] J. G. Boyd and D. C. Lagoudas. A thermodynamic constitutive model for shape memory material: 1. the monolithic shape memory alloy. *Int. J. Plast.*, 12:843–873, 1996.
- [18] L. C. Brinson and M. Panico. A three-dimensional phenomenological model for martensite reorientation in shape memory alloys. *J. Mech. Phys Solids*, 55:2491–2511, 2007.
- [19] L.C. Brinson, I. Schmidt, and R. Lammering. Stress-induced transformation behavior of a polycrystalline niti shape memory alloy: micro and macromechanical investigations via in situ optical microscopy. *J. Mech. Phys. Solids*, 52:1549–1571, 2004.
- [20] M. Brocca, L. C. Brinson, and Z. Bazant. Three-dimensional constitutive model for shape memory alloys based on microplane. *J. Mech. Phys Solids*, 50:1051–1077, 2002.
- [21] O. P. Bruno, F. Reitich, and P. H. Leo. The overall elastic energy of polycrystalline martensitic solids. *J. Mech. Phys. of Solids*, 44:1051–1101, 1996.
- [22] M. W. Burkart and T. A. Read. Diffusionless phase change in the indium-thallium system. *Trans. Amer. Inst. Mining and Metall. Eng.*, 197:1516–1254, 1953.
- [23] I. V. Chenchiah. *Energy-minimizing microstructures in multiphase elastic solids*. PhD thesis, California Institute of Technology, 2004.
- [24] M. Chipot and D. Kinderlehrer. Equilibrium configurations of crystals. *Arch. Rat. Mech. and Anal.*, 103:237–277, 1988.

- [25] B. D. Coleman and W. Noll. The thermodynamics of elastic materials with heat conduction and viscosity. *Arch. Rat. Mech. Anal.*, 13:167–178, 1963.
- [26] S. Daly, K. Bhattacharya, and G. Ravichandran. Stress-induced martensitic phase transformation in thin sheets of nitinol. *Acta Mater.*, 55:3593–3600, 2008.
- [27] K. Dayal and K. Bhattacharya. Kinetics of phase transformations in the peridynamic formulation of continuum mechanics. *Preprint*, pages 1–34, 2005.
- [28] P. W. Dondl. *Structure and evolution of martensitic phase boundaries*. PhD thesis, California Institute of Technology, 2007.
- [29] J. L. Ericksen. Some phase transitions in crystals. *Arch. Rat. Mech and Anal.*, 73:99–124, 1980.
- [30] J. D. Eshelby. The determination of the elastic field of an ellipsoidal inclusion, and related problems. *Proc. Royal Soc. London A*, 241:376–396, 1957.
- [31] S. Eucken and J. Hirsch. The effect of textures on shape memory behaviour. *Mat. Sci. Forum*, 56-58:487–492, 1990.
- [32] P. Feng and Q. P. Sun. Experimental investigation on macroscopic domain formation and evolution in polycrystalline niti microtubing under mechanical force. *J. Mech. Phys. Sol.*, 54:1568–1603, 2006.
- [33] S. Govindjee, A. Mielke, and G. J. Hall. The free energy of mixing for n-variant martensitic phase transformations using quasiconvex analysis. *J. Mech. Phys. Sol.*, 51:I–XXVI, 2003.
- [34] D. E. Hodgson, M. H. Wu, and R. J. Biermann. Shape memory alloys. Online at <http://www.sma-inc.com/SMAPaper.htm>, 2003.

- [35] M. Huang and L. C. Brinson. Multivariant model for single crystal shape memory. *J. Mech. Phys. Sol.*, 46:1379–1409, 1998.
- [36] Y. Jung. *Thin tube experiments and numerical simulations of micromechanical multivariant constitutive modeling in superelastic nitinol*. PhD thesis, University of California Berkeley, 2003.
- [37] R. Kohn. The relaxation of a double-well energy. *Cont. Mech, Thermodyn.*, 3:193–236, 1991.
- [38] R. V. Kohn and T. D. Little. Some model problems of polycrystal plasticity with deficient basic crystals. *SIAM J. Appl. Math.*, 59:172–197, 1998.
- [39] C. Lexcellent and P. Blanc. Phase transformation yield surface determination for some shape memory alloys. *Acta Mat.*, 52:2317–2324, 2004.
- [40] C. Lexcellent and M. R. Laydi. Yield criteria for shape memory materials:convexity conditions and surfaces transport. *Math. and Mech. of Solids*, To Appear, 2008.
- [41] C. Lexcellent, A. Vivet, C. Bouvet, S. Calloch, and P. Blanc. Experimental and numerical determinations of the initial surface of phase transformation under biaxial loading in some polycrystalline shape-memory alloys. *J. Mech. Phys. Solids*, 50:2717–2735, 2002.
- [42] AMT: Advanced Materials and Technologies. <http://www.amtbe.com>, 2008.
- [43] J. M. McNaney, V. Imbeni, Y. Jung, P. Papadopoulos, and R. O. Ritchie. An experimental study of the superelastic effect in a shape-memory nitinol alloy under biaxial loading. *Mechanics of Materials*, 35:969–986, 2003.

- [44] C. B. Morrey. Quasiconvexity and the semicontinuity of multiple integrals. *Pac. J. Math.*, 2:25–53, 1952.
- [45] G. B. Olson and W. S. Owen, editors. *Martensite*. ASM, 1992.
- [46] K. Otsuka and Wayman C. M. *Shape Memory Materials*. Cambridge University Press, 1998.
- [47] B. Peultier, B. T. Zineb, and E. Patoor. A simplified micromechanical constitutive law adapted to the design of shape memory applications by finite element methods. *Mat. Sci. and Eng. A*, 481-482:384–388, 2008.
- [48] R. Peyroux, A. Chrysochoos, C. Licht, and M. Lobel. Thermomechanical couplings and pseudoelasticity of shape memory alloys. *Int. J. Eng. Science*, 36:489–509, 1998.
- [49] A. C. Pipkin. Elastic materials with two preferred states. *Quart. J. Appl. Math.*, 44:1–15, 1991.
- [50] P. Purohit. *Dynamics of phase transitions in strings, beams, and atomic chains*. PhD thesis, California Institute of Technology, 2002.
- [51] R. T. Rockafellar. *Convex Analysis*. Princeton University Press, 1970.
- [52] T. Saburi and S. Nenno. The shape memory effect and related phenomena. In H. I. Aaronson, D. E. Laughlin, R. F. Sekerka, and C. M. Wayman, editors, *Proc. Int. Conf. on Solid-Solid Phase Transformations*, pages 1455–1479, New York, 1981. The Metall. Soc. AIME.
- [53] A. Sadjadpour. A micromechanics inspired constitutive model for shape-memory alloys: the one-dimensional case. *Smart Mater. Strut.*, 16:S51–S62, 2007.

- [54] A. Schlömerkemper. On a sachs bound for stress-induced phase transformations in polycrystalline shape memory alloys. *Proc. Appl. Math. Mech.*, Preprint, 2006.
- [55] I. Schmidt, L. C. Brinson, and R. Lammering. Micro and macromechanical observation of polycrystalline niti using in situ microscopy. *J. Phys. IV France*, 112:655–658, 2003.
- [56] J. A. Shaw and S. Kyriakides. On the nucleation and propagation of phase transformation fronts in a niti alloy. *Acta Metall.*, 45:683–700, 1997.
- [57] T.W. Shield. Orientation dependence of the pseudoelastic behavior of single-crystals of cu-al-ni in tension. *J. Mech. Phys. Solids*, 43:869–895, 1995.
- [58] Y.C. Shu and K. Bhattacharya. The influence of texture on the shape-memory effect in polycrystals. *Acta Mater.*, 46:5457–5473, 1998.
- [59] P. Sittner, Y. Hara, and M. Tokuda. Experimental study on the thermoelastic martensitic transformation in shape memory alloy polycrystal induced by combined external forces. *Metall. Mat. Trans.*, 26:2923–2935, 1995.
- [60] V. P. Smyshlaev and J. R. Willis. A "non-local" variational approach to the elastic energy minimization of martensitic polycrystals. *Proc. Roy. Soc. Lond. A*, 454:1573–1613, 1998.
- [61] Q. P. Sun and K. C. Hwang. Micromechanics modeling for the constitutive behavior of polycrystalline shape memory alloys: 1. derivation of general relations 2. study of individual phenomena. *J. Mech. Phys. Sol.*, 41:1–17, 19–33, 1993.

- [62] P.M. Suquet and K. Bhattacharya. Model problem concerning recoverable strains of shape-memory polycrystals. *Proc. Roy. Soc. Lond. A*, 461:2797–2816, 2005.
- [63] V. Sverak. Rank-one convexity does not imply quasiconvexity. *Proc. Royal Soc. Edinburgh A*, 120:185–189, 1992.
- [64] P. Thamburaja and L. Anand. Polycrystalline shape-memory materials: Effect of crystallographic texture. *J. Mech. Phys. Solids*, 49:709–737, 2001.